View metadata, citation and similar papers at core.ac.uk

brought to you by CORE

provided by NASA Technical Reports Server

FINAL REPORT- NASA GRANT NO. NAG3-1178

Numerical Procedures for Inlet/Diffuser/Nozzle Flows

Stanley G. Rubin, P.I.
(D. R. Reddy, Technical Monitor)

5/7/90-12/31/97

Department of Aerospace Engineering and Engineering Mechanics
P.O. Box 210070
University of Cincinnati
Cincinnati, OH 45221-0070

PRESSURE BASED FLUX-SPLIT SOLUTIONS FOR INCOMPRESSIBLE AND COMPRESSIBLE INTERNAL FLOWS

S. KAUSHIK[1] AND S. G. RUBIN[2]

Department of Aerospace Engineering and Engineering Mechanics
University of Cincinnati
Cincinnati, Ohio 45221

ABSTRACT

Two primitive variable, pressure based, flux-split, RNS/NS solution procedures for viscous flows are presented. Both methods are uniformly valid across the full Mach number range, i.e., from the incompressible limit to high supersonic speeds. The first method is an "optimized" version of a previously developed global pressure relaxation RNS procedure. Considerable reduction in the number of relatively expensive matrix inversion, and thereby in the computational time, has been achieved with this procedure. CPU times are reduced by a factor of 15 for predominantly elliptic flows (incompressible and low subsonic). The second method is a time-marching, 'linearized' convection RNS/NS procedure. The key to the efficiency of this procedure is the reduction to a single LU inversion at the inflow cross-plane. The remainder of the algorithm simply requires back-substitution with this LU and the corresponding residual vector at any cross-plane location. This method is not time-consistent, but has a convective-type CFL stability limitation. Both formulations are robust and provide accurate solutions for a variety of internal viscous flows to be provided herein.

1) Shailendra Kaushik, Project Engineer, EASi Engineering, 30800 Telegraph Rd., Suite 3700, Bingham Farms, Michigan 48025

2) Prof. Stanley G. Rubin, Aerospace Engineering, University of Cincinnati, Cincinnati, OH-45221-0070

1. INTRODUCTION

Various asymptotic approximations to the complete Navier-Stokes (NS) equations have been used to provide detailed, efficient and accurate flowfield descriptions for a significant class of large Reynolds number (Re) flows [1-5]. If these approximations are combined in a single system of composite equations, the resulting time-dependent system is termed the Reduced Navier-Stokes approximation (RNS). The RNS system in appropriate (ξ,η,ζ) coordinates is such that only streamwise or ξ diffusion terms in the full NS equations are higher order and therefore neglected throughout the flow domain. These terms are retained in a deferred corrector (DC) which may be recovered when necessary. The lowest order RNS approximation consists of the full Euler equations plus all the boundary-layer diffusion terms required to satisfy appropriate no-slip boundary conditions on various solid boundaries. In this manner, all acoustic (elliptic) influences contained in the full Navier Stokes (NS) equations, are retained. The resulting RNS system allows for upstream or elliptic influence and contains all the dominant physics associated with large Reynolds number strong viscous-inviscid interactions. A pressure based flux-splitting procedure is applied to the Euler component of these equations. This leads to a global relaxation procedure for the pressure, and for velocities in reverse flow regions. The convective and acoustic fluxes are treated independently. Therefore, the appropriate domain of dependence is automatically represented by the differencing of the convective and acoustic (pressure) gradients.

Two efficient, primitive variable RNS/NS solution procedures, valid across the full Mach number range, are presented in this paper. The primary features of these solvers are (a) that the boundary conditions and discretization procedure are controlled by the physics of the of the lowest order terms of the RNS system; (b) that the higher order diffusion, DC terms,in the NS system can be introduced if necessary in the final RNS inversion to obyain the full NS solution; (c) that they possess sharp shock capturing properties: within three grid points; (d) unlike other Euler-based Navier-Stokes methods, that become unconditionally unstable in the incompressible limit, these formulations perform efficiently for all Mach numbers from incompressible to high supersonic and; (e) a pressure velocity flux-split discretization is implemented in both of these solvers.

The first of the RNS/NS solvers is an optimized version of a global pressure relaxation RNS procedure previously presented [1-3]. The main drawback of the original algorithm is the cumulatively high number of expensive LU of cross-plane coefficient matrix inversions that are required. At least three non-linear Newton iterations or LU inverions are needed at each cross-plane. For three-dimensional (3D), turbulent flows, wherein fine grids are needed to resolve the thin boundary layers, the matrix inversions become computationally expensive and impacts adversely on the efficiency and speed of the solution procedure. One of the primary goals of the present study is to minimize this cost. Toward this end various optimizational techniques are adopted: (a) recast the governing equations in "delta" form, so that a single LU inverse at a given cross-plane can be applied as an approximate LU for several subsequent stations downstream; (b) global under-relaxation of flow variables, with time terms in the governing equations (c) local under-relaxation of the flow variables during the non-linear iterations and; (d) a judicious initialization of flow variables at a given cross plane with those computed at a preceding station in the prior sweep. With these techniques considerable reduction in the required number of LU inversions, and consequently in the computational time results. For instance, the optimized version of the code runs about 15 times faster than the original "unoptimized" procedure for laminar, incompressible flow in a 90^{0} curved duct, and a 33x41x41 grid. The optimized code requires a single LU inverse to attain a steady-state solution. This compares with 174 inverions per sweep for the original version. In this particular case, 32 global sweeps are required to converge the maximum residuals to the prescribed tolerance level. Note, that it requires exactly "imax-1" number of global sweeps for incompressible flows to converge to machine accuracy; where "imax" is the number of stations in the streamwise direction, as the downstream pressure boundary condition traverses a single grid cell for every pass.

The second algorithm, i.e., 'linearized' convection model, is a time-marching RNS procedure. This is a straightforward algorithm that involves just a single LU inverse at the inflow cross-plane. The method marches in pseudo-time with the application of a single back-substitution, for the LU inverse and the corresponding residual vector at each cross-plane, during a given sweep. With this mathematical operation, all the flow variables are

marched a single time-step in a given sweep. Note, that this procedure is not time-consistent. This process of time-marching, is repeated until a steady-state is attained. A convection-only CFL type time-limitation, discussed in reference [4-5] for the time consistent algorithm, is applicable for this method. Since flow variables at all cross-plane locations can be marched a single time-step simultaneously i.e., they are fully uncoupled numerically in the axial or flow direction, this procedure lends itself to parallelization. This method is particularly efficient for incompressible and low subsonic Mach numbers. For supersonic flows, the "optimized' pressure relaxation procedure is more suitable and therefore preferred.

Both methods implement a pressure velocity flux-split discretization [1-3]. The RNS/NS system of equations is quasi-linearized and discretized as described previously in [4,5]. A system of simultaneous algebraic equations (for the cross-plane in three dimensions) is solved with a sparse matrix direct solver (SMDS). The use of this solver is dictated by robustness and consistency considerations discussed in previous papers [1-3].

Both methods have been validated through a series of three-dimensional internal flow configurations: (a) Laminar and turbulent, incompressible flow in an S-shaped duct; (b) laminar and turbulent, compressible flow in a symmetric, square cross-section choked convergent-divergent nozzle and, (c) turbulent, supersonic flow in a generic inlet geometry.

The algebraic Baldwin-Lomax eddy viscosity model, modified to include multiple wall effects, is employed for turbulence closure.

2. GOVERNING EQUATIONS

The reduced form of the Navier-Stokes (RNS) equations is employed for both of the flow solvers considered herein. All higher order axial diffusion terms are retained only in the deferred-corrector (DC). The DC is explicitly introduced in the final RNS inversion to obtain a full NS solution, see ref. [10]

In order to obtain the final RNS system of equations, the full NS equations are transformed from Cartesian into non-orthogonal generalized curvilinear coordinates in strong conservation form. These are as follows:

Continuity:

$$\frac{\partial}{\partial t}\left(\frac{\rho}{J}\right)+\frac{\partial}{\partial \xi}\left(\frac{\rho U}{J}\right)+\frac{\partial}{\partial \eta}\left(\frac{\rho V}{J}\right)+\frac{\partial}{\partial \zeta}\left(\frac{\rho W}{J}\right)=0 \tag{1}$$

X-momentum equation:

$$\frac{\partial}{\partial t}\left(\frac{\rho u}{J}\right)+\frac{\partial}{\partial \xi}\left(\frac{\rho U u}{J}\right)+\frac{\partial}{\partial \eta}\left(\frac{\rho V u}{J}\right)+\frac{\partial}{\partial \zeta}\left(\frac{\rho W u}{J}\right)+\xi_x\frac{\partial P}{\partial \xi}+\eta_x\frac{\partial P}{\partial \eta}+\zeta_x\frac{\partial P}{\partial \zeta}=$$
$$\frac{\partial}{\partial \xi}\left(\frac{\tau_x^{\xi}}{J}\right)+\frac{\partial}{\partial \eta}\left(\frac{\tau_x^{\eta}}{J}\right)+\frac{\partial}{\partial \zeta}\left(\frac{\tau_x^{\zeta}}{J}\right) \tag{2}$$

Y-momentum equation:

$$\frac{\partial}{\partial t}\left(\frac{\rho v}{J}\right)+\frac{\partial}{\partial \xi}\left(\frac{\rho U v}{J}\right)+\frac{\partial}{\partial \eta}\left(\frac{\rho V v}{J}\right)+\frac{\partial}{\partial \zeta}\left(\frac{\rho W v}{J}\right)+\xi_y\frac{\partial P}{\partial \xi}+\eta_y\frac{\partial P}{\partial \eta}+\zeta_y\frac{\partial P}{\partial \zeta}=$$
$$\frac{\partial}{\partial \xi}\left(\frac{\tau_y^{\xi}}{J}\right)+\frac{\partial}{\partial \eta}\left(\frac{\tau_y^{\eta}}{J}\right)+\frac{\partial}{\partial \zeta}\left(\frac{\tau_y^{\zeta}}{J}\right) \tag{3}$$

Z-momentum equation:

$$\frac{\partial}{\partial t}\left(\frac{\rho w}{J}\right)+\frac{\partial}{\partial \xi}\left(\frac{\rho U w}{J}\right)+\frac{\partial}{\partial \eta}\left(\frac{\rho V w}{J}\right)+\frac{\partial}{\partial \zeta}\left(\frac{\rho W w}{J}\right)+\xi_z\frac{\partial P}{\partial \xi}+\eta_z\frac{\partial P}{\partial \eta}+\zeta_z\frac{\partial P}{\partial \zeta}=$$
$$\frac{\partial}{\partial \xi}\left(\frac{\tau_z^{\xi}}{J}\right)+\frac{\partial}{\partial \eta}\left(\frac{\tau_z^{\eta}}{J}\right)+\frac{\partial}{\partial \zeta}\left(\frac{\tau_z^{\zeta}}{J}\right) \tag{4}$$

Energy equation (constant total enthalpy):

$$T = 1 + \frac{\gamma - 1}{2} M_\infty^2 (1 - q^2) \tag{5}$$

Equation of State:

$$T = \frac{\gamma M_\infty^2 P}{\rho} \tag{6}$$

By eliminating temperature T from the equations (5) and (6), the following relationship is obtained:

$$\rho = \frac{2\gamma M_\infty^2 P}{2 + (1-\gamma) M_\infty^2 (1 - q^2)} \tag{7}$$

It is this form of combined energy equation and the equation of state that is used in the present study. In the incompressible limit, the non-dimensional density is set to unity. The viscous terms, viz, τ_x^ξ, τ_y^ξ, τ_x^η, τ_y^ζ , etc., appearing on the right-hand-side (RHS) in equations 1-4 have been discussed previously in [6]. The definitions of the metric quantities, e.g., ξ_x, ξ_y, η_x, ζ_y, etc., and the contravariant velocities U, V, and W appearing in these equations have also been defined in [6]. The RNS set of equations are obtained from the full NS equations by simply dropping the higher order diffusion (ξ-derivatives) terms. These are retained in the DC. The final form of the momentum equations used in these solvers are obtained by taking the covariant momentum balances in the ξ,η,ζ directions.

3. DISCRETIZATION

The pressure velocity flux-split technique, originally developed by Rubin and Lin [1,7], is applied to the RNS equations in generalized non-orthogonal curvilinear coordinates. Fig.1 depicts the discretization location of the equations and their appropriate groupings, at a typical cross-plane, of a given axial station $\xi=\xi_i$. The ξ-momentum and the energy equations are discretized at the grid points. The continuity equation is cell centered and the η and ζ-momentum equations are located at the half points. All ξ-derivatives in the continuity equation are backward differenced and the cross-flow (η,ζ) derivatives are two-point trapezoidal differenced. All axial convection terms in the momentum equations are upwind or flux-vector differenced and the cross-flow convection terms are either 3-point central differenced or two-point trapezoidal differenced. This depends on the location at which these derivatives are discretized. All diffusion terms are second order accurate three-point central differenced. The streamwise pressure gradient P_ξ in the ξ-momentum equation is flux split into positive and negative contributions in accordance with the pressure flux-vector splitting technique [1]:

$$P_\xi = \omega(P_\xi)_{Hyperbolic} + (1-\omega)(P_\xi)_{Elliptic}$$

or

$$P_\xi = \omega_{i-\frac{1}{2}}\left(\frac{P_i - P_{i-1}}{\Delta\xi}\right) + (1-\omega_{i+\frac{1}{2}})\left(\frac{P_{i+1} - P_i}{\Delta\xi}\right)$$

or equivalently

$$P_\xi = \frac{\overline{P}_i - \overline{P}_{i-1}}{\Delta\xi} \qquad (8)$$

where $\overline{P}_i$ is located at the same grid location as the velocity u_i, and is given, to second order in $\Delta\xi$, by

$$\overline{P}_i = \omega_{i+\frac{1}{2}} P_i + (1-\omega_{i+\frac{1}{2}}) P_{i+1} \tag{9}$$

For constant stagnation enthalpy, the variable ω in the above equations is given as

$$\omega \le \min\left\{1, \frac{\gamma M_\xi^2}{1+(\gamma-1)M_\xi^2}\right\}$$

where (10)

$$M_\xi = \frac{U}{a} = \frac{u\xi_x + v\xi_y + w\xi_z}{a(\xi_x^2+\xi_y^2+\xi_z^2)^{1/2}}$$

In equation (8) the term $\omega(P_\xi)_{Hyperbolic}$ or $\omega_{i-\frac{1}{2}}\left(\frac{P_i - P_{i-1}}{\Delta\xi}\right)$ reflects the initial value or the parabolic/hyperbolic component in the streamwise pressure gradient. The term $(1-\omega)(P_\xi)_{Elliptic}$ or $(1-\omega_{i+\frac{1}{2}})\left(\frac{P_{i+1} - P_i}{\Delta\xi}\right)$ reflects the upstream influence or the boundary value or the elliptic component of the pressure gradient. The discretization of P_ξ implies that the "unknown" pressure P_i at the axial (marching) location i, is staggered at a distance $(1-\omega)\Delta\xi$ upstream of the velocity u_i, v_i, and w_i. The pressure $\overline{P}_i$ at the grid point i is given by eqn. (9). In the incompressible limit, ω=0, and the pressure at the grid point *i* is $\overline{P}_i = P_{i+1}$. For supersonic flows, ω=1 and $\overline{P}_i = P_i$. By neglecting the negative flux contribution of the streamwise pressure gradient, i.e. by retaining only the hyperbolic component in P_ξ

$P_\xi = \omega_{i-\frac{1}{2}}\left(\frac{P_i - P_{i-1}}{\Delta\xi}\right)$, the multiple-sweep global pressure relaxation RNS formulation reduces to the single-sweep PNS (Parabolized Navier-Stokes) formulation. The discretization of cross-flow pressure gradients P_η and P_ζ in the η-momentum and the ζ-

momentum equations is quite straightforward and is given by two-point trapezoidal differencing.

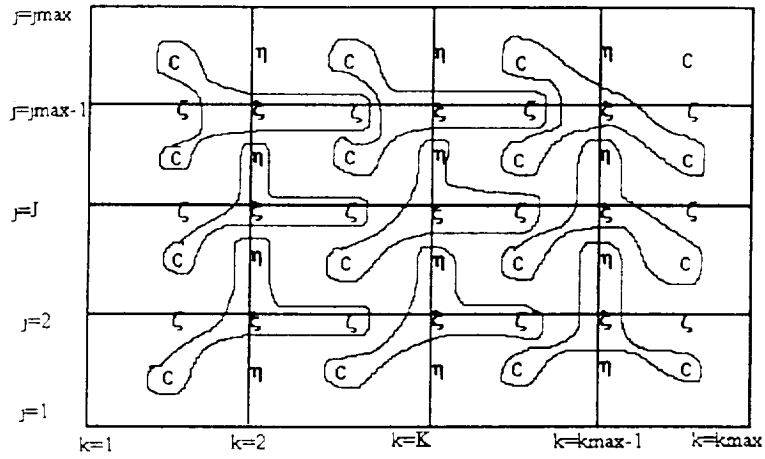

Fig.1 Implementation of boundary condition in a ξ_i cross-plane for an internal flow geometry.

4. BOUNDARY CONDITIONS

The appropriate boundary conditions, consistent with the discretized system of RNS equations, are as follows:

inflow boundary $(\xi = \xi_{in})$*:*

In the "streamwise" or ξ direction, at the inflow boundary, all flow variables or ξ derivatives are prescribed as follows:

$u = u_{in}(\eta,\zeta)$

$v = v_{in}(\eta,\zeta)$

$w = w_{in}(\eta,\zeta)$

$M = M_{in}$ (zero for incompressible flow)

$\rho = \rho_{in}(\eta,\zeta)$

$P_{\xi\xi} = 0$ (for internal, compressible flow)

For incompressible flow calculations, the inflow pressure is not prescribed, but is calculated from $\bar{P}_{i-1} = P_i$. For subsonic flows, the pressure $\bar{P}_{i-1}$ as defined by eqn. (9), still retains some influence of the prescribed inflow solution P_{i-1}. In these calculations the value of $\bar{P}_{i-1}$ changes to reflect the upstream pressure influence, see Rosenbaum and Rubin [8]. This allows for adjustment of inflow mass through changes in P_i and hence ρ_{in}.

outflow boundary $(\xi = \xi_{out})$:

At a subsonic or incompressible outflow, $0 \leq M_{\xi} < 1$, without flow reversal, only the pressure or pressure gradient is required. For the PNS "supersonic" step, the negative pressure fluxes are not present, and therefore, the pressure is calculated at this boundary. Due to the presence of a "subsonic" boundary layer region, even in supersonic viscous flow cases, the pressure at the exit boundary, computed from the PNS step, is prescribed as the outflow pressure boundary condition for subsequent RNS steps.

For zero flow reversal at the outflow, the velocities are calculated from the solver.

For small reverse flow at the exit, the velocities can be prescribed from available experimental data, or computed by neglecting the negative velocity flux at the outflow boundary. This is similar to a FLARE approximation used in boundary layer theory. For the present study, the FLARE approximation is applied only at the outflow boundary.

wall boundary:

No slip and zero-injection *(u=0, v=0, w=0)* for viscous flow computation.

Zero-vorticity condition for inviscid/Euler computation.

Pressure is computed at all wall grid points using the special regroupings discussed in [4,5].

The density is computed at all wall points from the constant stagnation enthalpy condition.

free boundaries (external flow):

The inplane velocities, pressure and density are specified. The *velocities normal to the free boundary* are computed.

5. SOLUTION PROCEDURE

For both procedures considered herein, the discrete system of fully coupled RNS system in generalized, non-orthogonal, curvilinear coordinates, at a given cross-plane, is written in the following *delta* form: $[A]\{\delta x\}^{n+1} = (r)^n$; where $[A]$ represents the sparse cross-plane coefficient matrix; $\{\delta x\}^{n+1}$ represents the solution vector in *delta* form and $(r)^n$ is the right-hand-side residual vector, evaluated at a previous time or iteration. Since the primary goal is to drive the local cross-plane residuals to a prescribed tolerance level, an "exact" inverse of $[A]$ is not required. An approximate LU that is "close-enough" in character to the exact one is found sufficient. In other words, in *delta* form, an exact LU of the coefficient matrix at an arbitrary cross-plane, can successfully drive the residuals, at several subsequent "streamwise" stations, to an acceptable level of accuracy. Furthermore, if the "optimizational" techniques, mentioned in the Introduction of this paper, are implemented appropriately, then just a *single* LU of the coefficient matrix, at the inflow cross-plane, has been found to be sufficient for the entire computation. Although, this might result in an increased number of back-substitutions to resolve local non-linearities, the overall cost is considerably reduced. Back-substitution operations, with an

approximate LU, is applied iteratively until the local non-linearities are resolved and the local residuals have achieved a prescribed tolerance level. If during this iterative back-substitution process the residuals show signs of growth, or if the local convergence of non-linearities become excessively slow, a new LU is initiated. In addition, the number of required LUs can be further reduced with the aid of under-relaxation, both globally (inclusion of time-terms) and locally. This process of back-substitution and LU decomposition is continually repeated until there is local convergence of all residuals at all the axial stations, in a given sweep. Multiple sweeps are generally required to converge all residuals globally.

For the linearized convective time-marching RNS procedure, only one LU inverse at the inflow cross-plane is required. This linearizes the non-linear terms about the prescribed inflow conditions. Unlike the global pressure relaxation procedure, the non-linearities are not resolved locally but in a global fashion. A single back-substitution operation is required at any given axial cross-plane for all axial sweeps. As a result, all the flow variables in the computational domain evolve in pseudo-time through a single time-step. This process is repeated until steady-state conditions are attained. A convection-only CFL limitation is applicable, see ref. [4-5].

Fig. 2 depicts the comparison of convergence histories for the linearzied convection, time-marching model and the fully-implicit, pressure relaxation procedure. The flow problem under consideration is an incompressible, laminar flow in an S-duct at Re=790. The grid has 31 stations in the axial direction and 21x21 in a cross-plane. As seen in the figure, the convergence history for the linearized convection model shows a more gradual downward trend than the pressure relaxation model. However, the computational time required by both methods to converge to a steady-state is about the same i.e., approximately 50 minutes on a RISC/6000 workstation. As noted earlier, apart from the difference in time-steps used in the two methods, the linearized convection model does not converge non-linearities at each axial location. This is required in the pressure relaxation procedure. The gain in time by the former method is clearly outweighed by the need for a larger number of axial sweeps or "time-steps" for convergence.

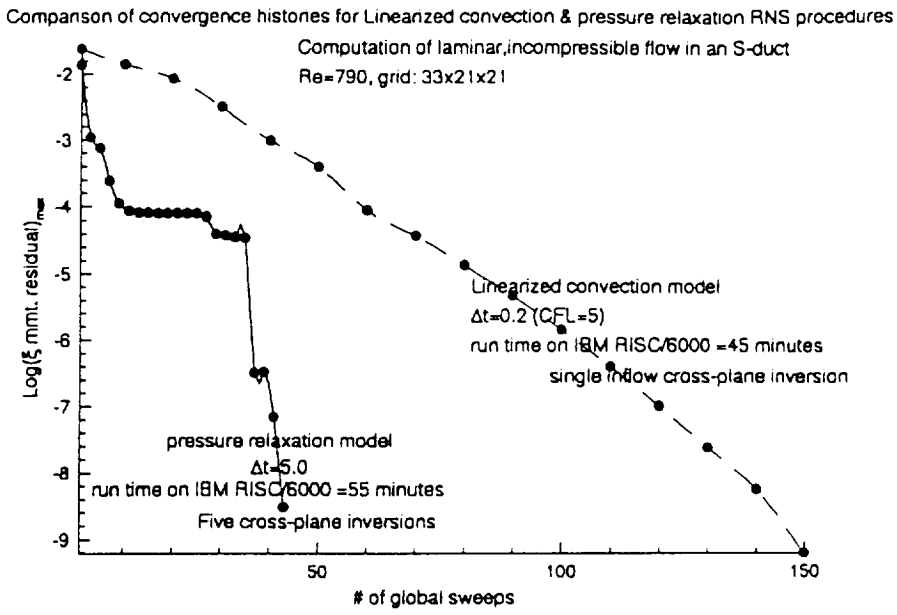

Fig. 2 Comparison of convergence histories for the Linearized convection model and the pressure relaxation procedure for a laminar, incompressible flow in an S-duct.

Both procedures are quite robust and have been implemented in the same code. This provides the flexibility to switch from one algorithm to the other for a given flow problem in a single run.

6. RESULTS

In order to validate these RNS/NS flow solvers, a variety of 3D internal flow configurations, ranging in speed from the incompressible limit to high supersonic Mach number, have been investigated. An algebraic, zero-equation Baldwin-Lomax model, modified to handle multiple walls, has been applied in all the turbulent flow cases.

Incompressible flow in an S-shaped duct: Incompressible flow in an S-shaped duct of constant area square cross-section is investigated. Two flow Reynolds numbers are considered, Re=790 (laminar) and Re=40,000 (turbulent). A combination of the linearized convection and the 'optimized' global pressure relaxation solvers is applied. The numerical results are compared with the measurements of Taylor et al. [9]. The secondary flow phenomena in a S-duct is mainly pressure driven because of the very smooth-bend in the

walls. Axial flow separation is not observed. Accurate prediction of the boundary layer, even in the laminar case, is required to capture the small but complex secondary flows. The grid in the cross-plane must be adequately refined in order to correctly predict this behavior. Grids with 33 axial stations and with 31x31 or 41x41 points in the cross-plane are prescribed for the laminar and turbulent cases, respectively. The symmetry plane grid for the turbulent case is shown in Fig.3 The linearized convection code is applied in the initial phase of the computation to drive the maximum residuals down to 0.01. Thereafter, the "optimized" fully implicit relaxation solver, with infinite time step, is automatically initiated. In this mode, the residuals reach the prescribed levels of tolerance, typically 0.0001, relatively fast. The convergence history of the laminar computation is depicted in Fig.4.

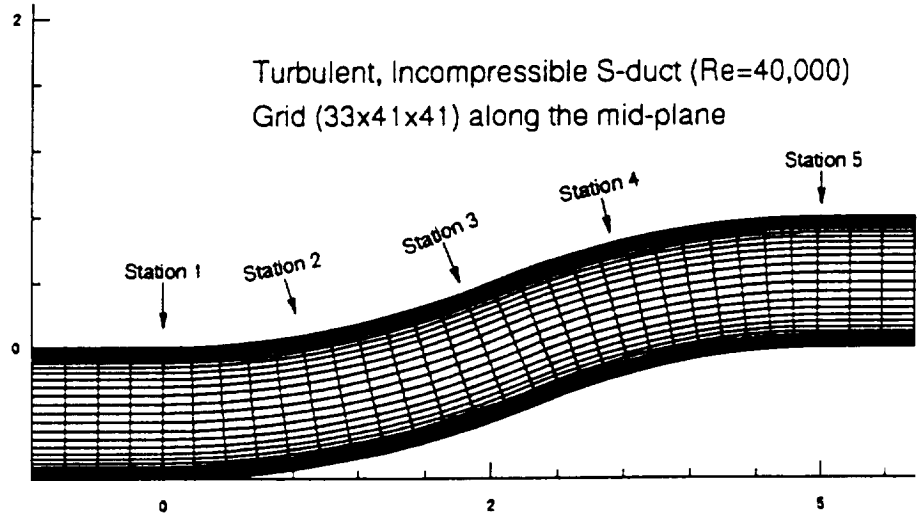

Figure 3. Typical view of the geometry and the grid in the symmetry plane

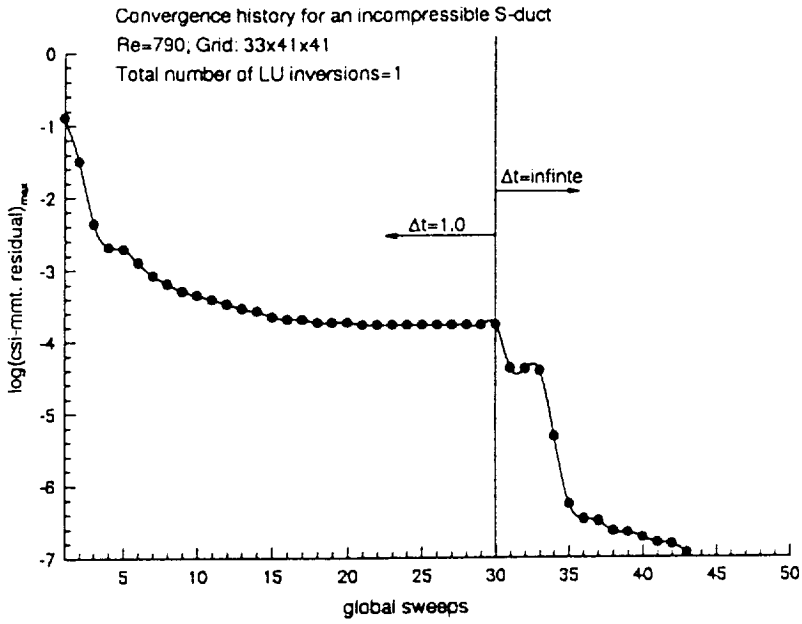

Fig 4. Convergence history for a laminar, incompressible flow in an S-duct

The streamwise velocity profiles, for both laminar and turbulent flows, on the symmetry/midplane of the S-duct, is compared with the measured data of Taylor et al. [9]. Results at several axial stations, shown in Figs. 5(a-e) and Figs. 6(a-e), are depicted. There is an excellent agreement with the experimental data for both laminar and turbulent flows. This computation requires about 4 hours for the laminar and about 6 hours for the turbulent case on the RISC/6000 machine. This is roughly equivalent (without vectorization) to 30 and 50 minutes, respectively, on a Cray YMP supercomputer.

In order to demonstrate the effect of the reduction in the required number of LU inversions on the computational time, a laminar incompressible case was considered. A single LU inversion is required by the "optimized" version of the global pressure relaxation solver, while 174 LUs are required by the original code during each axial sweep. Since the number of global sweeps approximately equals the number of nodes in the axial direction, this results in an enhancement of almost 15.

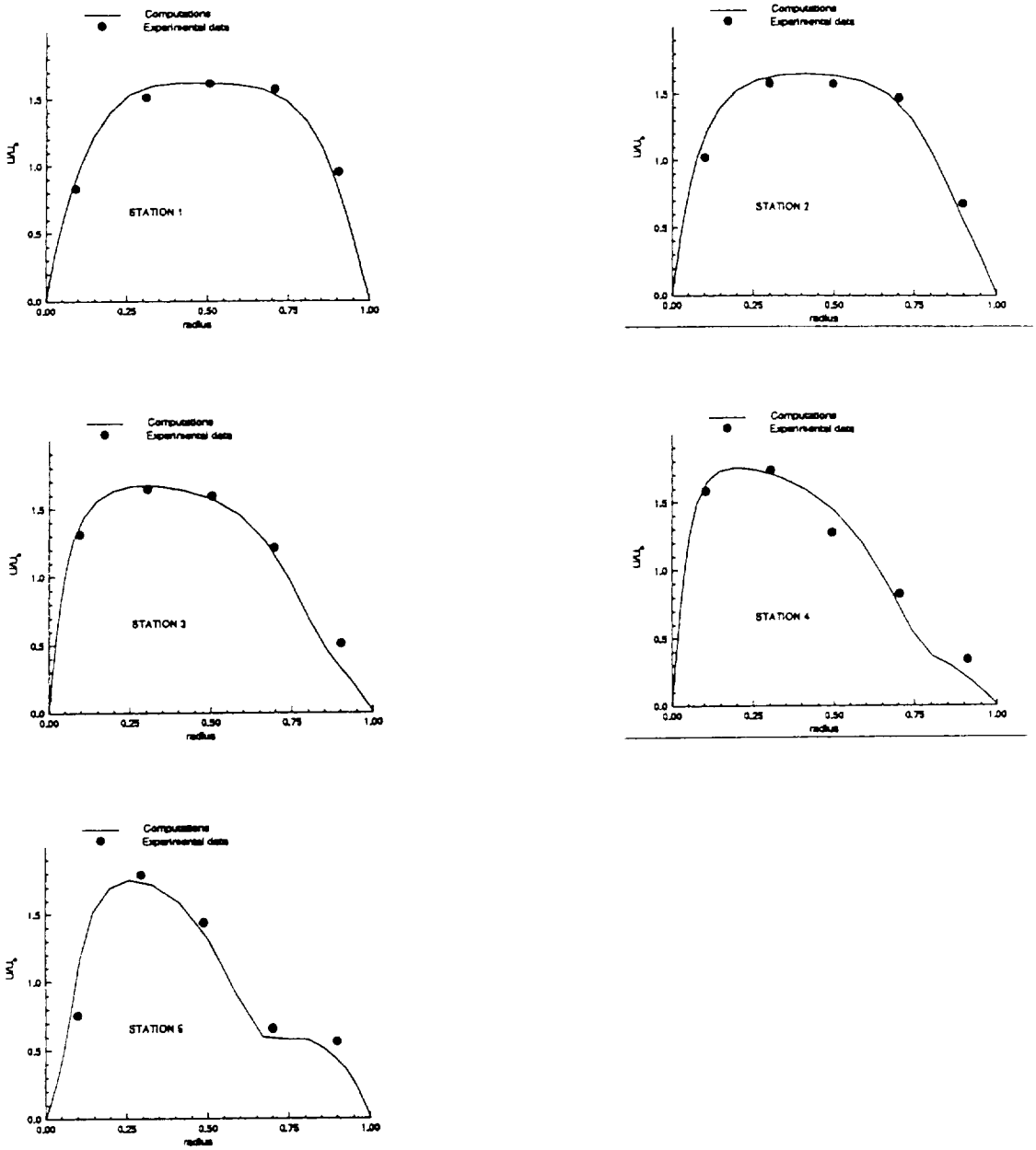

Figures 5(a-e). Comparison of the laminar axial velocity profiles on the symmetry plane at stations 1-5 along an S-duct

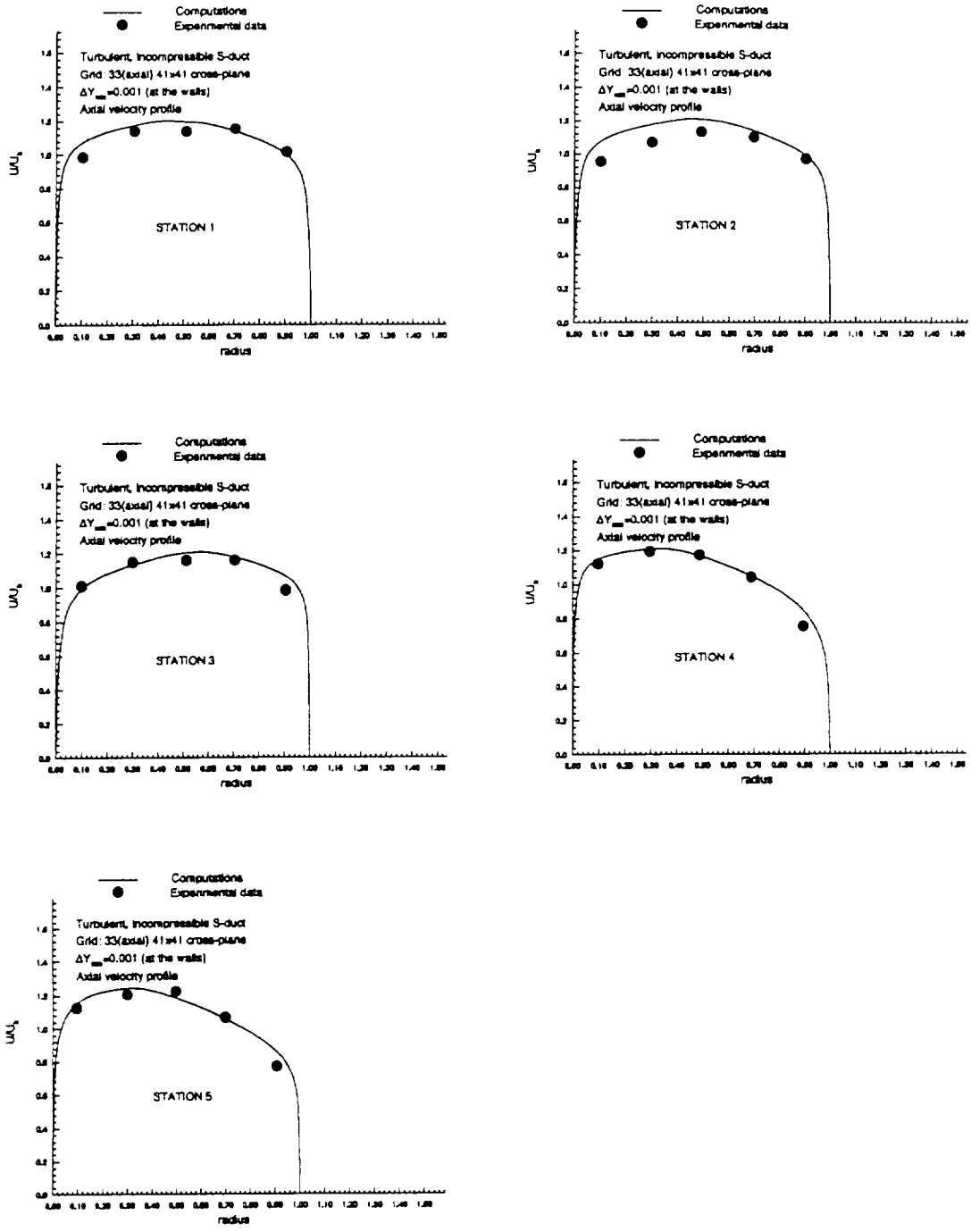

Figures 6(a-e). Comparison of the computed and measured turbulent axial velocity profiles for an S-duct

*(b) **Turbulent, 3D convergent-divergent choked nozzle:*** Turbulent flow in a symmetric, convergent-divergent nozzle, with square cross-section, and an area ratio, $A_{inlet}/A_{throat}=3.41$, is computed with the linearized convection procedure. The Reynolds number is $Re=5x10^5$ based on the throat diameter. This computation is for design point conditions, so that the pressures are prescribed at both ends of the nozzle in accordance with the results of quasi-1D analysis. A Mach number of 0.2 is prescribed at the inlet. As expected, the nozzle is choked with a Mach number of unity at the geometric throat. At the exit cross-plane, an average Mach number of 2.8 is computed. This is in excellent agreement with quasi-1D thoery. A grid with 31 axial stations and a highly stretched 41x41 mesh in the cross-plane is employed. Figs.7-8 depict the Mach number and pressure contours on a symmetry plane. The computed Mach number ratio between the inlet and the exit are in close agreement with quasi-1D analysis.

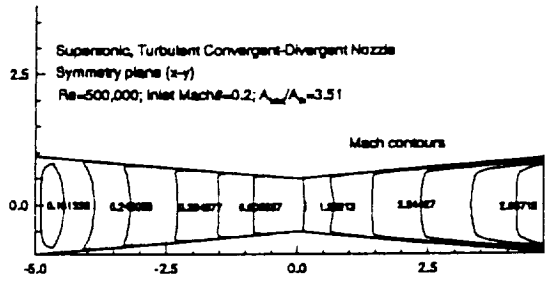

Figure 7. Mach number contours on a symmetry plane

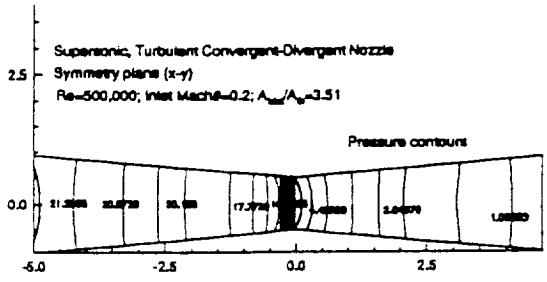

Figure 8. Non-dimensional pressure contours on a symmetry plane

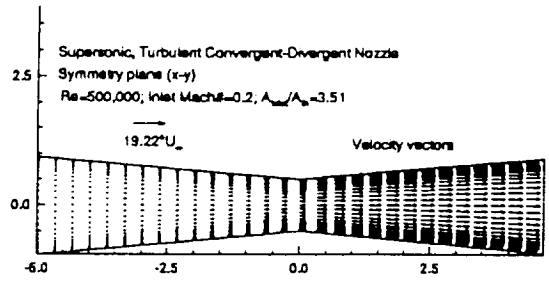

Figure 9. Velocity vectors on a symmetry plane

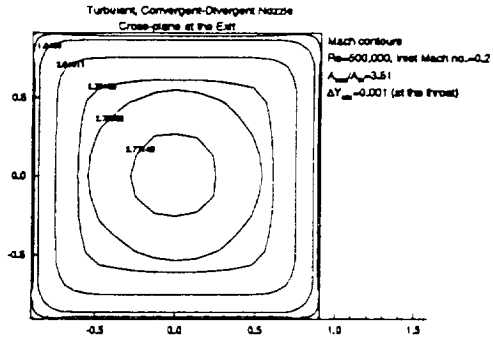

Figure 10(a). Mach number at the exit cross-plane.

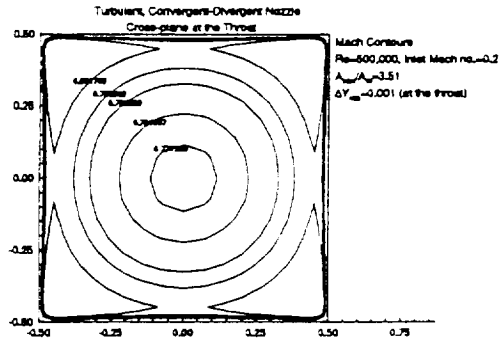

Figure 10(b). Mach number at the throat cross-plane.

Fig.9 depicts velocity vectors on a symmetry plane, and Figs.10(a-b) depict Mach number at the exit and throat axial stations, respectively. Note, that unlike other NS flow solvers, there is *no* deterioration in computational performance in the lower spectrum of Mach number.

(c) Effect of back-pressure on a laminar, compressible flow through a choked convergent-divergent Nozzle: In order to study the effect of the back-pressure, 'p_b', on the performance of a convergent-divergent nozzle, a laminar flow at Re=500 is considered. The nozzle is identical to the one considered for the turbulent case. The grid has 51 axial stations and 33x33 nodes in a cross-plane. Mild stretching, of about 1.1 at the walls, is applied. This was adequate to resolve a relatively thick boundary layer associated with the lower Re. In this study, a series of computations with different back pressures at the exit was carried out. The first calculation was for a steady-state solution at design conditions, i.e., $p_b=p_e$ (complete expansion). Here 'p_e' denotes the exit pressure that would be attained under design conditions. From quasi-one-dimensional theory, the pressure ratio p_e/p_{in} for design conditions is approximately 27 for an area ratio A_e/A_{throat} of 3.51. Subsequently, the back-pressure is raised in a gradual fashion. First, the back-pressure is increased to $p_b=3.6p_e$ and a steady-state solution is obtained for this condition with the design-point solution as an initial guess. Next, the back-pressure is further increased to $p_b=6.25p_e$ and again a steady-state solution is obtained with the previously obtained steady-state solution at $p_b=3.6p_e$ applied as the starting solution. For this back-pressure, axial flow separation associated with oblique shock formation is predicted. In order to assess the effect of area ratio A_e/A_{throat}, the flare angle of all the walls in the divergent section of the nozzles is then reduced from 5 to 3 degrees. This decreases the area ratio A_e/A_{throat} from 3.51 to 2.3. The convergent section of the nozzle is not altered. The design point pressure ratio, p_e/p_{in}, for the modified nozzle geometry is reduced to about 13.5 from quasi-one-dimensional analysis. The final imposed back-pressure, previously 6.25 times the design exit pressure in the original nozzle geometry, now reduces to 3.37 of the design exit pressure i.e., $p_b=3.37p_e$. A steady-state solution is now obtained for the modified nozzle. For this calculation, the steady-state solution associated with the original nozzle and $p_b=6.25p_e$, is applied as the starting solution. As expected the reverse flow regions, that were present in the original design no

longer exists for the modified nozzle case. This provides a rapid tool for nozzle design studies. This computation required only 2 hours on RISC6000.

Subsequent to the design point computation, only divergent portion of the nozzle need to be evaluated. As long as the nozzle remains choked any increment in the back-pressure does not affect the flow conditions upstream of the throat. Therefore, each steady-state solution, at higher back-pressures, was obtained relatively inexpensively. It took approximately 7 hours on the IBM RISC/6000 machine for the design condition computation. Each subsequent run took only about 2.5-3 hours. This translates to approximately 50 and 18-23 minutes, respectively, on a Cray YMP supercomputer.

The effect of higher back-pressure on the pressure, skin friction, axial velocity and cross-flow velocity is depicted in Figs. 11-14. For $p_b=p_e$ or $p_e/p_{in}=27$, complete or optimal expansion takes place. For $p_b=3.57p_e$ or $p_e/p_{in}=7$, axial flow separation is imminent. This is visible from the skin friction coefficient along the lower wall in Fig. 12. Only a slight adverse pressure gradient is evident. As the back-pressure is further increased to $p_b=6.25p_e$ or $p_e/p_{in}=4$, two strong oblique shocks are generated. Behind these shock waves the flow separates and the pressure increases to the imposed back-pressure. Since the core the flow is supersonic, the effect of increased back-pressure is propagated upstream through the subsonic boundary layers close to the wall. The skin friction and axial velocity clearly show the existence of the reverse flow region. Fig.15 shows the streamlines in the (x-y) symmetry plane, wherein reverse flow regions are clearly evident. Fig.16 depicts the streamlines in the (x-y) symmetry plane for the modified nozzle. As expected, the shock induced reverse flow regions disappear.

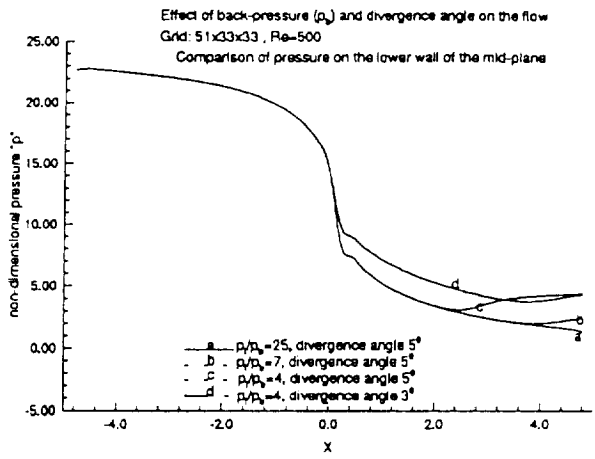

Figure 11 Comparison of pressure on the lower wall of the symmetry plane for various imposed back-pressures

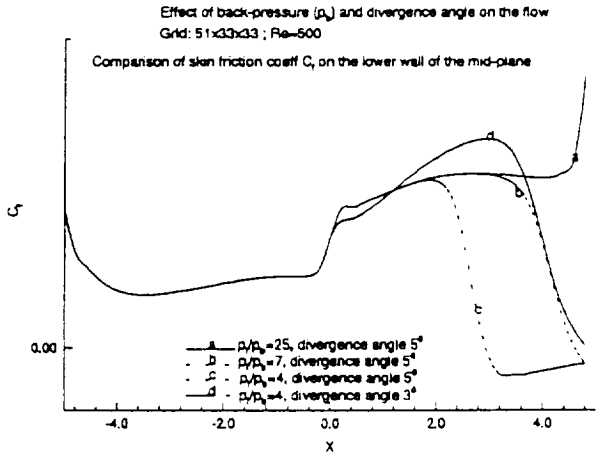

Figure 12 Comparison of skin friction coefficient C_f on the lower wall of the symmetry plane for various imposed back-pressures

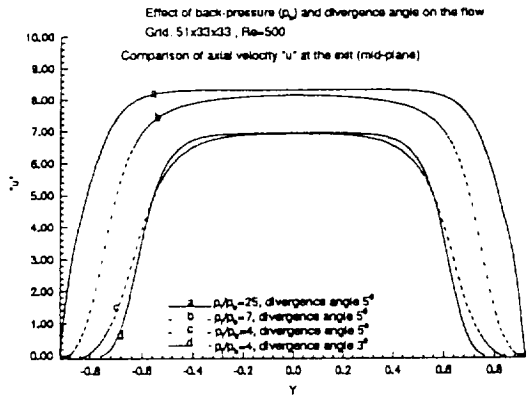

Figure 13 Comparison of axial velocity "u" at the exit cross-plane for various imposed back-pressures

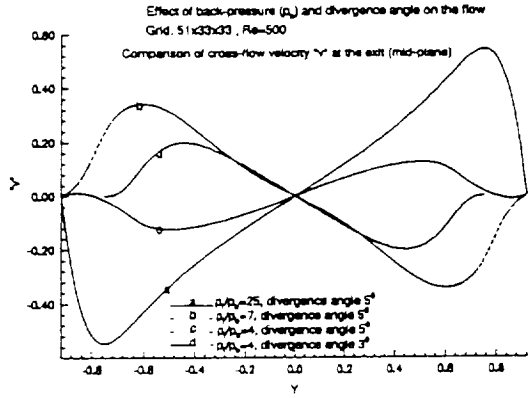

Figure 14 Comparison of cross-flow velocity "v" at the exit cross-plane for various imposed back-pressures

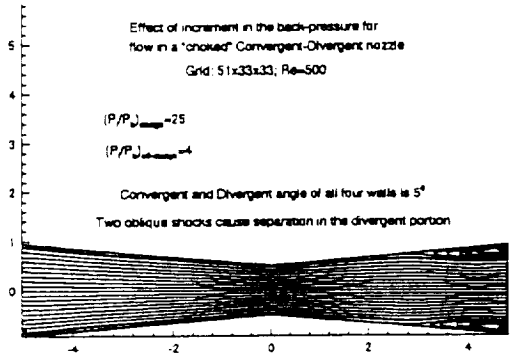

Figure 15 Streamlines on the (x-y) symmetry plane for the imposed back-pressure of $p_b=6.25p_e$ & A_e/A_{throat} of 3.51

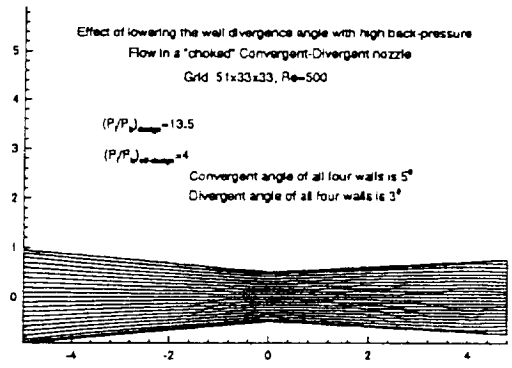

Figure 16 Streamlines on the (x-y) symmetry plane for the imposed back-pressure of $p_b=3.37p_e$ & A_e/A_{throat} of 2.3

Grid Convergence and Accuracy: In order to assess grid convergence and accuracy of these calculations, three grids, 31x17x17, 31x33x33 and 51x33x33, with refinement in all three directions, were considered. Calculations were performed at design conditions for a laminar, compressible flow. Although Figures 17-20 suggest further grid refinement in all three directions to obtain grid independence, the solution obtained on the finest grid 51x33x33 can be considered reasonably accurate. All plots, except pressure, show significant disparity between the solution obtained with a coarse 31x17x17 grid and that obtained with finer 31x33x33 and 51x33x33 grids. The pressure, however, is not affected by grid refinement. This is due to a predominantly inviscid nature of the flow. However, the accuracy of velocities and skin friction calculation is enhanced by clustering more grid points in the boundary layer. The effect of axial refinement is minimal on skin friction. It, however, increases the peak slightly of both, axial and cross-flow components of the velocity. The skin friction appears to be affected solely by refinement in the cross-plane.

After an initial decline in the skin friction, due to a developing boundary layer, it continuously increases throughtout the length of the nozzle. Both, skin friction and pressure plots, suggest an accelerating flow in the nozzle. Faster accleration rates are seen in the divergent section. A sudden expansion near the throat is evident in the pressure plot. This is also reflected in the increment of skin friction in the proximity of the throat. The axial velocity maximum occurs closer to the walls than the center line. This is seen in the

axial velocity plot of Fig. 19. The reason being the existence of extremely thin boundary layers on the four adjacent walls, caused by a tremendous flow acceleration, that do not interact with each other in the central core region. As a result, a large portion of the core flow remains inviscid.

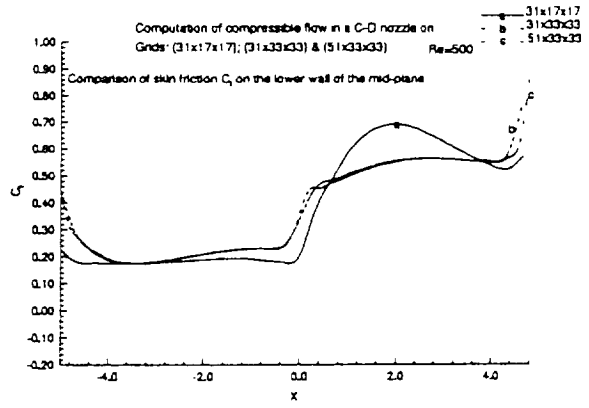

Figure 17 Skin friction coefficient C_f on the lower wall of the (x-y) symmetry plane for 31x17x17, 31x33x33 and 51x33x33 grids

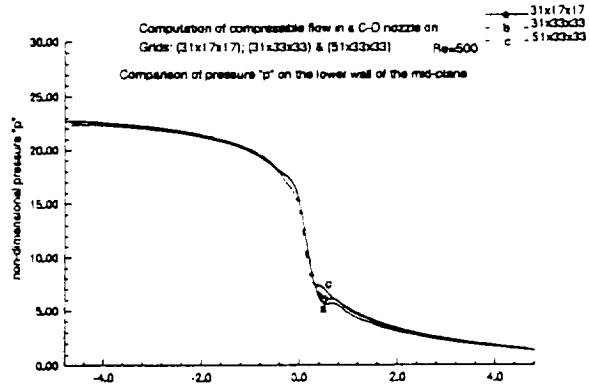

Figure 18 Non-dimensional pressure on the lower wall of the (x-y) symmetry plane for 31x17x17, 31x33x33 and 51x33x33 grids

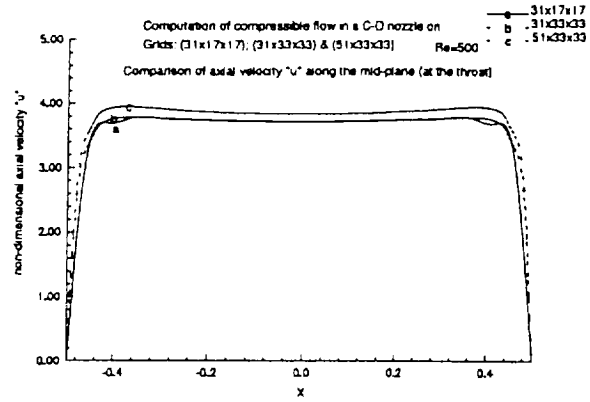

Figure 19 Axial velocity "u" at the throat for 31x17x17, 31x33x33 and 51x33x33 grids

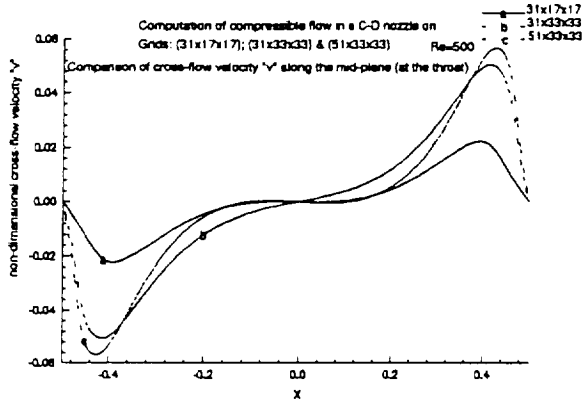

Figure 20 Cross-flow velocity "v" at the throat for 31x17x17, 31x33x33 and 51x33x33 grids

(d) Turbulent, Supersonic flow in a Generic Three-dimensional, 10^0 single-ramp inlet:

Turbulent, supersonic flow, in a generic three-dimensional, 10° single-ramp inlet geometry is investigated with the 'optimized' solver. The inlet Mach number is $M_{inlet}=3.0$ and the Reynolds number is $Re=5x10^5$. Efficient simulation of complex shock patterns in such internal configurations is examined. The grid in a symmetry plane is shown in Fig.21. In order to study grid dependency and accuracy of the solution, computations were carried out on three different grids. Although, grids I and II have same dimensions, i.e., 41 nodes in the axial direction and 41x41 in the cross-flow directions, the first node in the straight

duct portion of the inlet for grid I is 0.002 away from the walls as opposed to 0.0008 in grid II. Grid III has the same dimensions and distribution of mesh points in the grid II cross-plane, but has 61 nodes in the axial direction. On average, the computation on a 41x41x41 grid takes about 45 minutes per global pressure relaxation sweep on a RISC/6000 workstation. This is equivalent to about 6 minutes on a Cray YMP supercomputer. A total of about 6 global sweeps are required to converge all the residuals to the tolerance level of 0.0001.

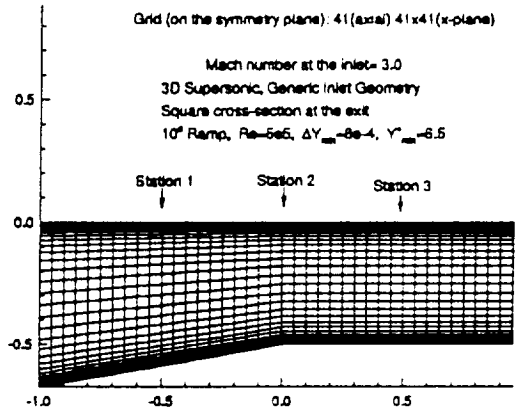

Figure 21. Typical view of the grid in the symmetry plane

Figs.22(a-d) depict the axial "u" and cross-flow velocity "v" profiles along the symmetry plane at axial stations 1 and 2. Solutions on all three grids have been used for this comparison. There are no noticeable changes in "u", and for "v" there are only minor differences.

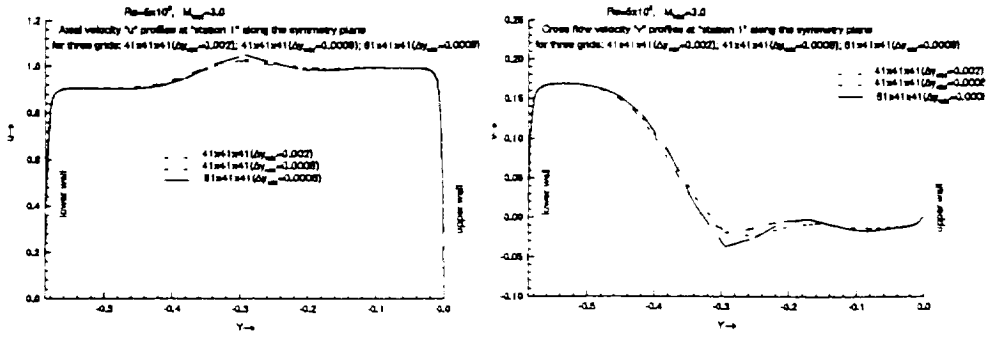

Figure 22(a-b). "u" and "v" velocity profiles at "station 1" along the mid-plane

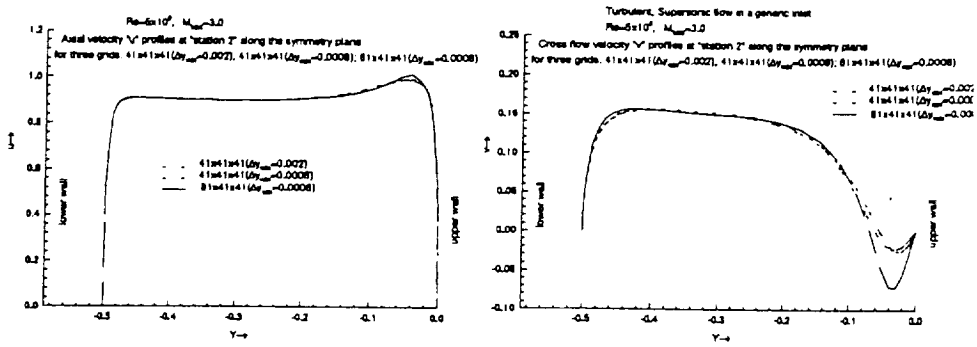

Figure 22(c-d). "u" and "v" velocity profiles at "station 2" along the mid-plane

Figs.23(a-b) depict the non-dimensional pressure on the symmetry plane lower and upper walls. With reference to Fig.23(a), the higher pressure level, behind the strong oblique shock, remains practically constant to the point where the ramp becomes horizontal (x=1.0). A steep decline in the pressure profile at this point is due to an expansion fan generated at the convex corner, x=1.0. Further downstream of this point, the pressure profile shows a slight tendency to rise. This is due to the impingement of the reflected oblique shock from the upper to the lower wall in the vicinity, x=1.9. Since the intensity of the doubly reflected shock is considerably diffused at this point, the rise in pressure is comparatively small.

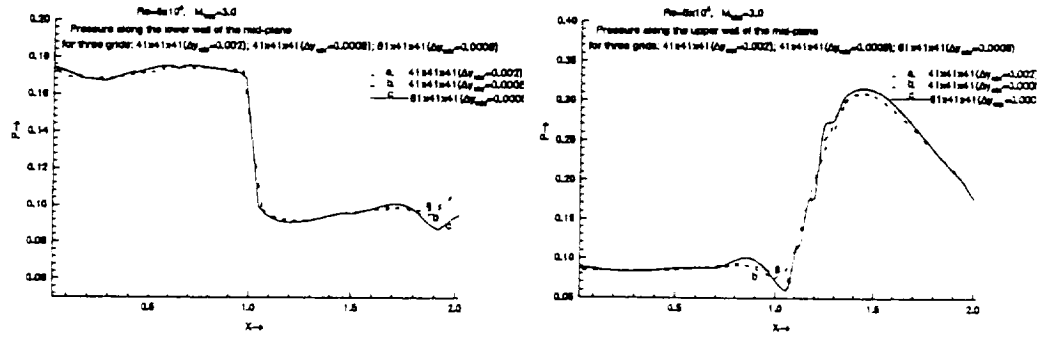

Figure 23(a-b). Non-dimensional pressure on the lower and upper walls, respectively, along the symmetry plane

Fig.23(b) depicts the pressure on the upper wall along the symmetry plane. In the region, $0.0 \leq x \leq 1.0$, the pressure on the upper wall remains fairly constant. The strong oblique shock, that originates at the beginning of the ramp (x=0.0 at lower wall), impinges the upper wall at x=1.0. This causes an adverse pressure gradient in the region, $1.0 \leq x \leq 1.4$. If this negative pressure gradient is sufficiently high, it can cause flow reversal. Subsequently, in the range, $1.4 \leq x \leq 2.0$ (exit), a steady drop in pressure is observed. This can be attributed to the influence of the expansion fan, that originates from x=1.0 on the lower wall and interacts with the reflected shock. This complex interaction of shock wave, expansion fan and boundary layer is seen in Figs.24(a-b).

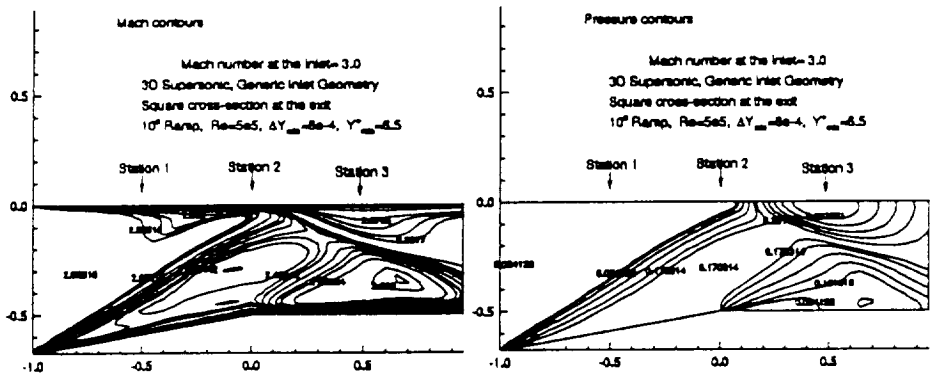

Figure 24(a-b). Mach number and non-dimensional pressure contours on the symmetry plane

7. CONCLUSIONS

The validity of two primitive variable RNS/NS flow solvers, for calculations from the incompressible limit to supersonic speeds has been demonstrated. The required number of LU inversions has been significantly reduced for the global pressure relaxation procedure. As a result, a speed-up of almost 15 has been achieved for an incompressible laminar flow in a S-shaped duct. For non-separated supersonic flows, this method is even more efficient. The efficiency and the validity of the time-marching, linearized convection model presented herein, has also been validated with S-duct, and convergent-divergent choked nozzle computations. Agreement with the data has been quite good thoughout.

ACKNOWLEDGMENTS

This work has been supported in part by NASA Grant NAG I3-1178.

REFERENCES

(1) Rubin, S. G., Tannehill, J. C., Parabolized/Reduced Navier-Stokes Computational Techniques. *Annu. Rev. Fluid. Mech.* : 117-144, 1992

(2) Rubin. S. G., Khosla, P. K., A review of reduced Navier-Stokes computations for compressible viscous flows, *Journal of Computers and Systems Engineering*, vol. 1, 549-62.

(3) Pordal, H. S., Khosla, P. K., Rubin, S. G., A flux-split solution procedure for unsteady inlet flows, *AIAA 90-0585,* 1990.

(4) Kaushik, S., Rubin, S. G., Khosla, P. K., Direct Primitive Variable Incompressible Solution for Two and Three Dimensional Viscous Flows. *AIAA 93-3004,* 1993.

(5) Kaushik, S., Rubin, S. G., Incompressible Navier-Stokes Solutions with a New a Primitive Variable Solver. *Computer and Fluids,* 24, 1, 27-40, 1995.

(6) Reddy, D. R., Rubin, S. G., Consistent Boundary Conditions for Reduced Navier-Stokes (RNS) Scheme Applied Three-Dimensional Viscous Flows. *J Fluid Mech. 60 part 1.* 105-127, 1988.

(7) Lin, A., Rubin, S. G., Viscous Flow over a cone at moderate incidences. I hypersonic tip region. *Computers and Fluids* 1: 37-57, 1973.

(8) Rosenbaum, D., Rubin, S. G., Global pressure relaxation for laminar two-dimensional internal flow, *International Journal of Numerical Methods in Fluids.* 10, 827-48, 1990.

(9) Taylor, A. M. K. P., Whitelaw, J. H., Yianneskis, M., Developing Flow in S-shaped Ducts , I-Square Cross-Section Duct. *NASA CR-3550,* 1982.

(10) Srinivasan, K., Rubin, S. G., Segmented multigrid domain decomposition procedure for incompressible viscous flows, *International Journal of Numerical Methods in Fluids.* 15, 1333-1335, 1992.

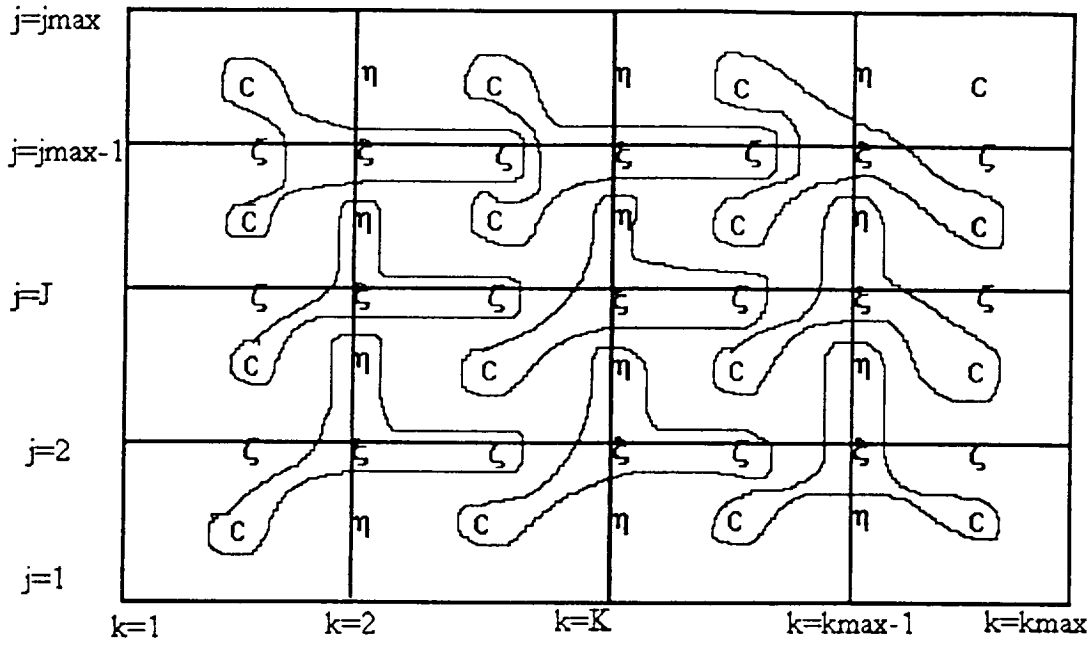

Fig.1 Implementation of boundary condition in a ξ_i cross-plane for an internal flow geometry.

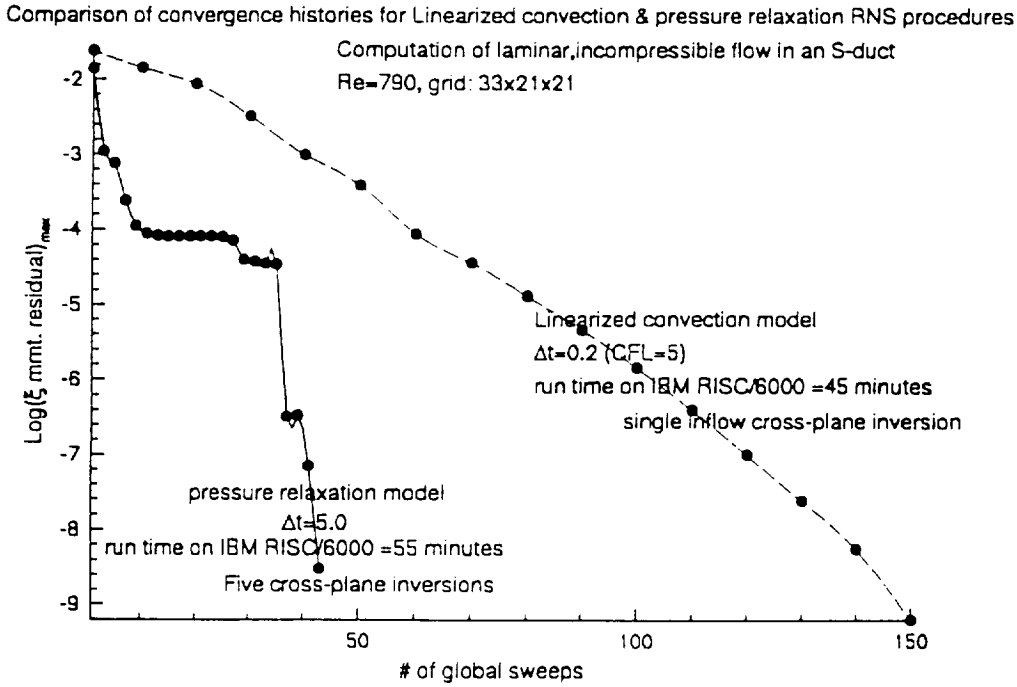

Fig. 2 Comparison of convergence histories for the Linearized convection model and the pressure relaxation procedure for a laminar, incompressible flow in an S-duct.

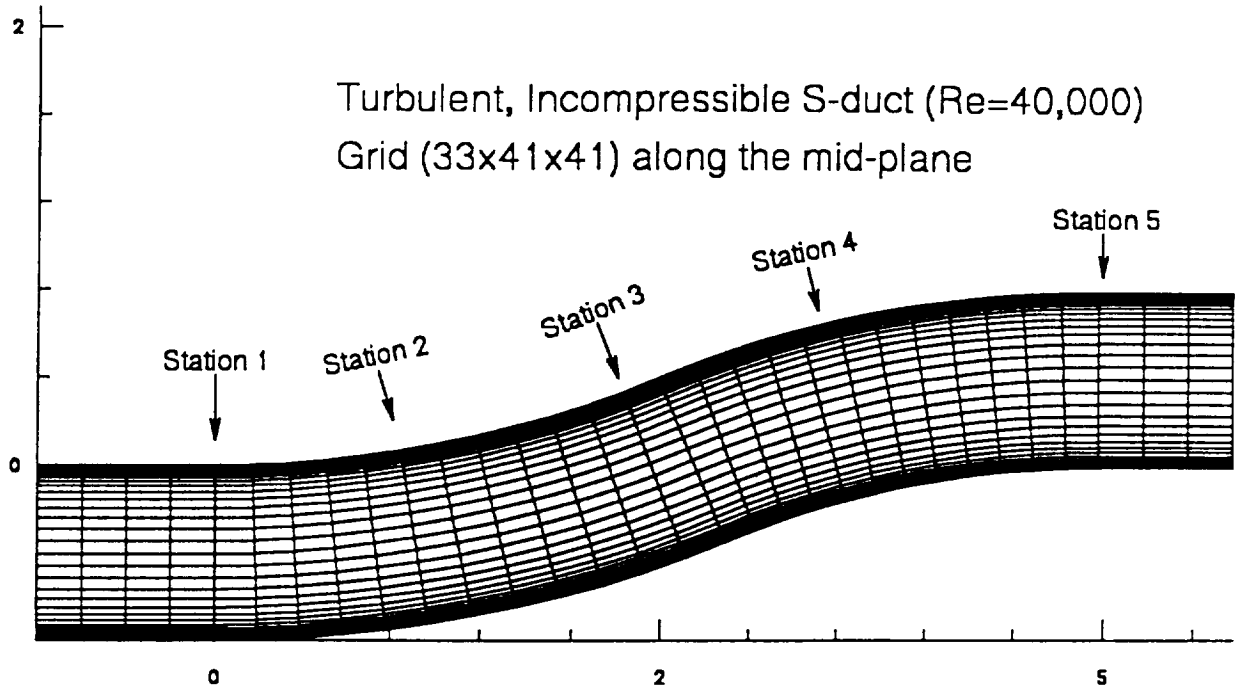

Figure 3. Typical view of the geometry and the grid in the symmetry plane

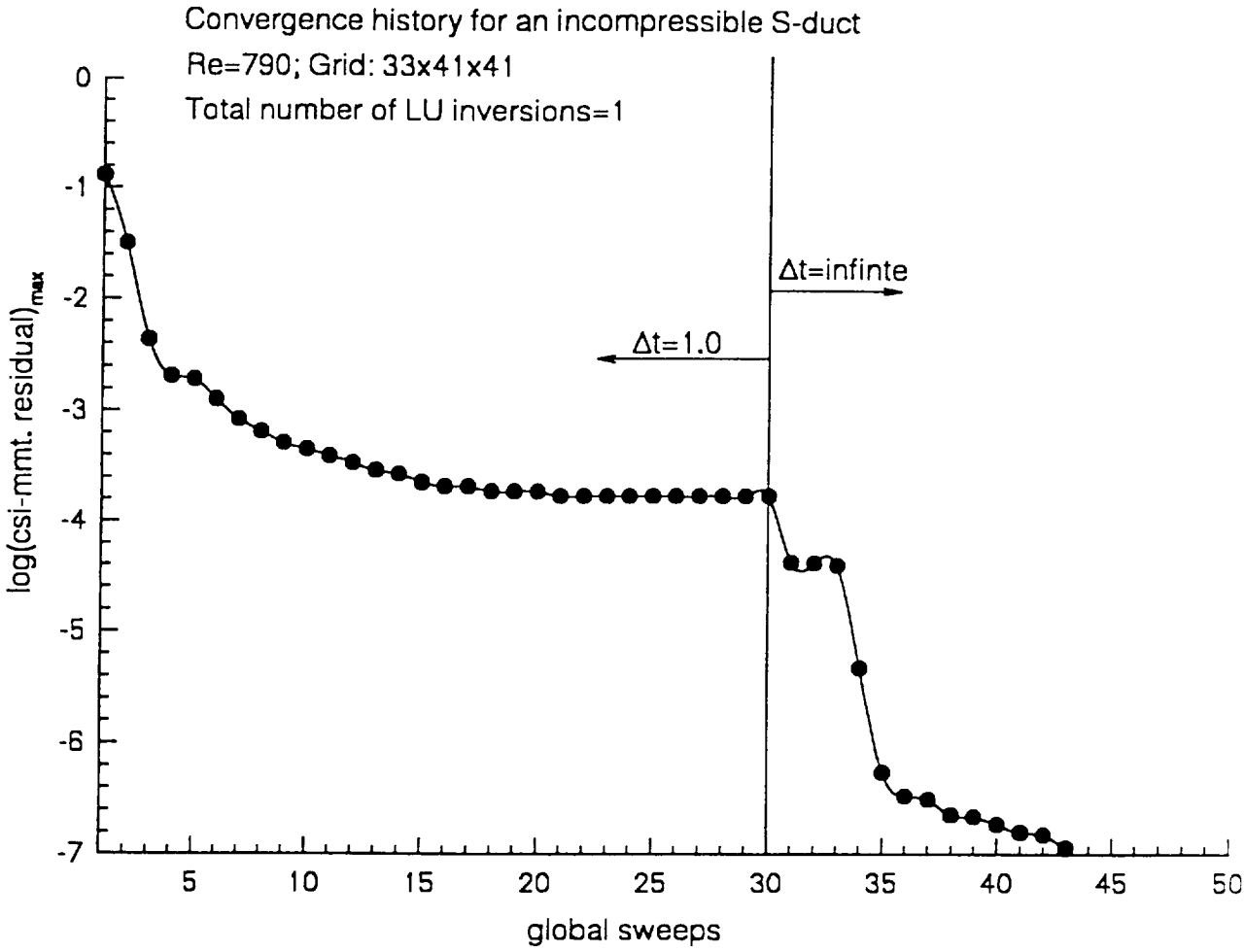

Fig 4. Convergence history for a laminar, incompressible flow in an S-duct

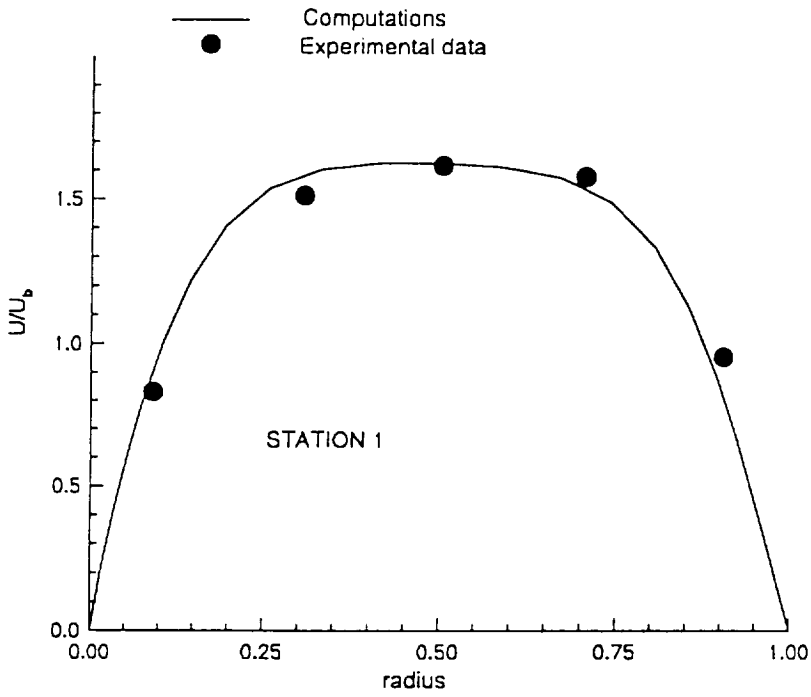
Computations
Experimental data
U/U_b
1.5
1.0
0.5
0.0
STATION 1
0.00
0.25
0.50
0.75
1.00
radius

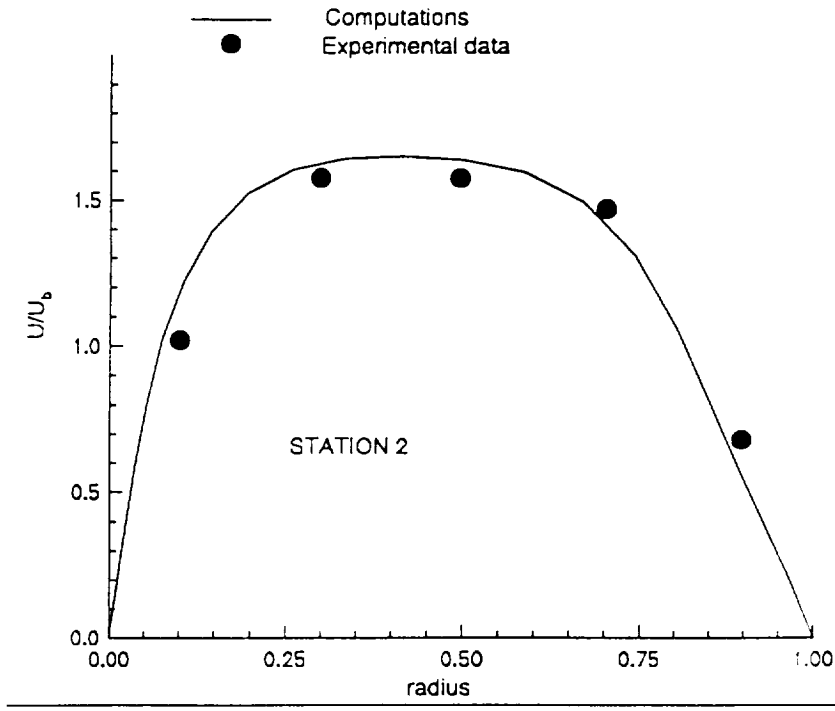
Computations
Experimental data
U/U_b
1.5
1.0
0.5
0.0
STATION 2
0.00
0.25
0.50
0.75
1.00
radius

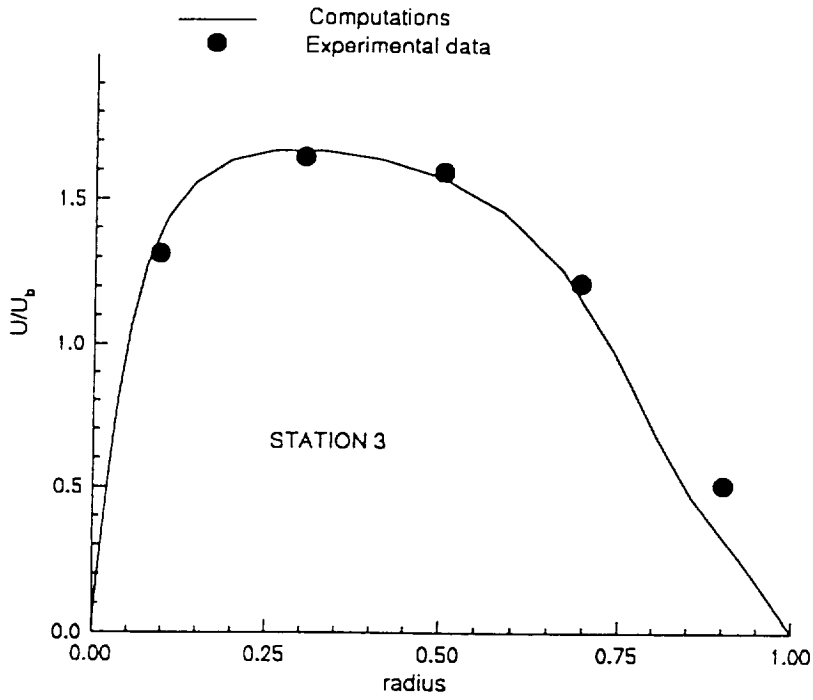
Computations
Experimental data
U/U_b
1.5
1.0
0.5
0.0
STATION 3
0.00
0.25
0.50
0.75
1.00
radius

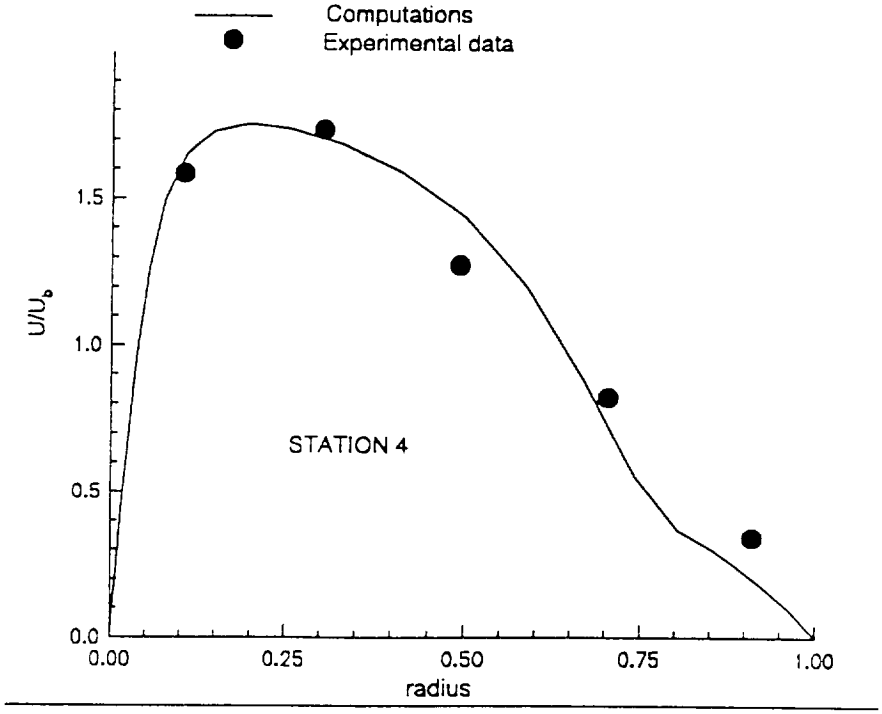
Computations
Experimental data
U/U_b
1.5
1.0
0.5
0.0
STATION 4
0.00
0.25
0.50
0.75
1.00
radius

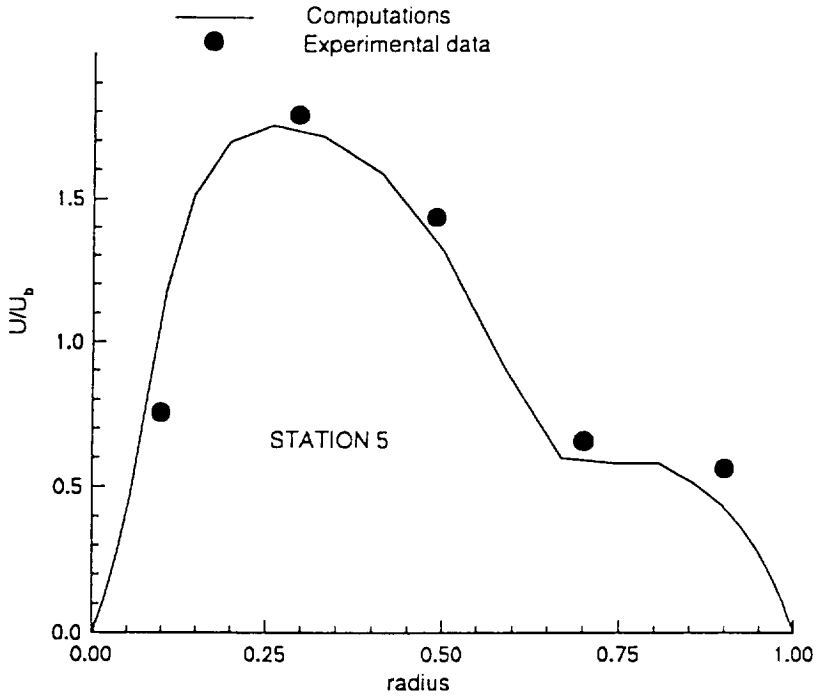

Figures 5(a-e). Comparison of the laminar axial velocity profiles on the symmetry plane at stations 1-5 along the S-duct

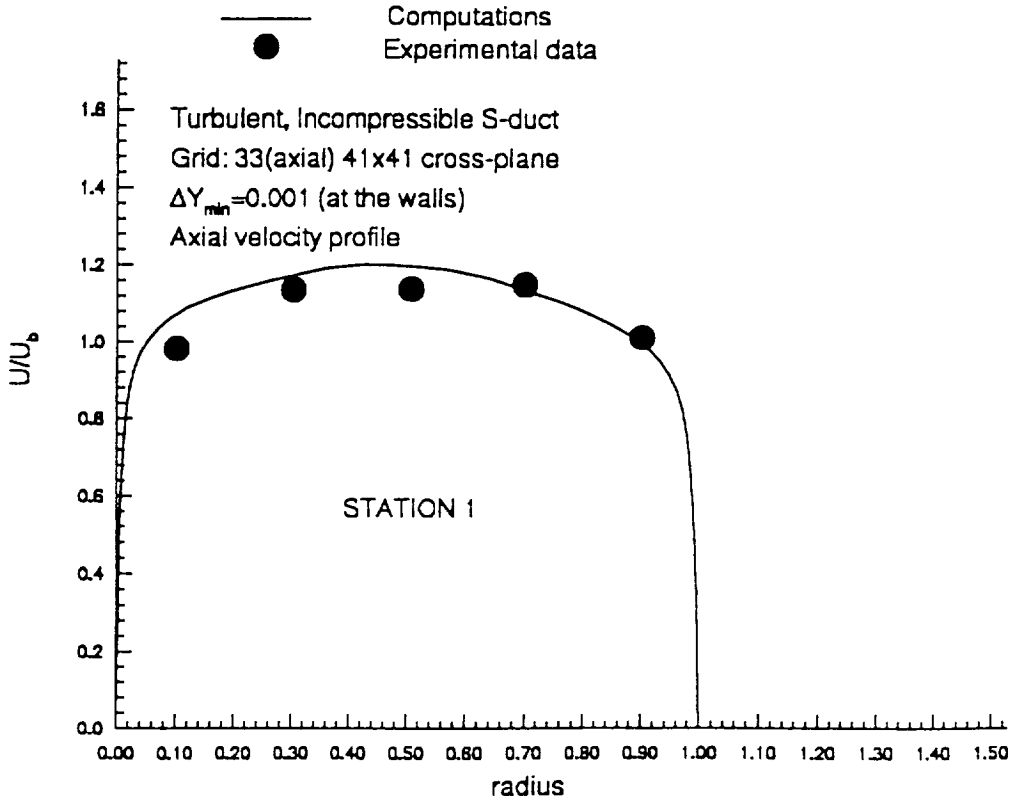

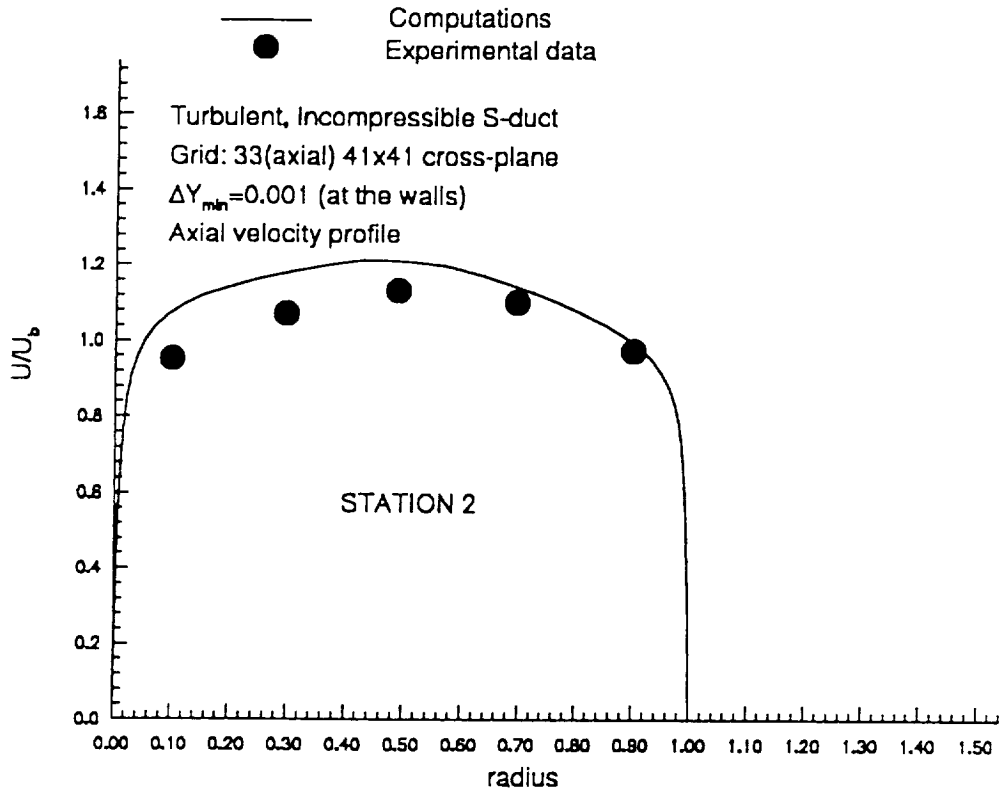
Computations
Experimental data
Turbulent, Incompressible S-duct
Grid: 33(axial) 41x41 cross-plane
ΔY_min=0.001 (at the walls)
Axial velocity profile
STATION 2
U/U_b
radius
0.0
0.2
0.4
0.6
0.8
1.0
1.2
1.4
1.6
0.00 0.10 0.20 0.30 0.40 0.50 0.60 0.70 0.80 0.90 1.00 1.10 1.20 1.30 1.40 1.50

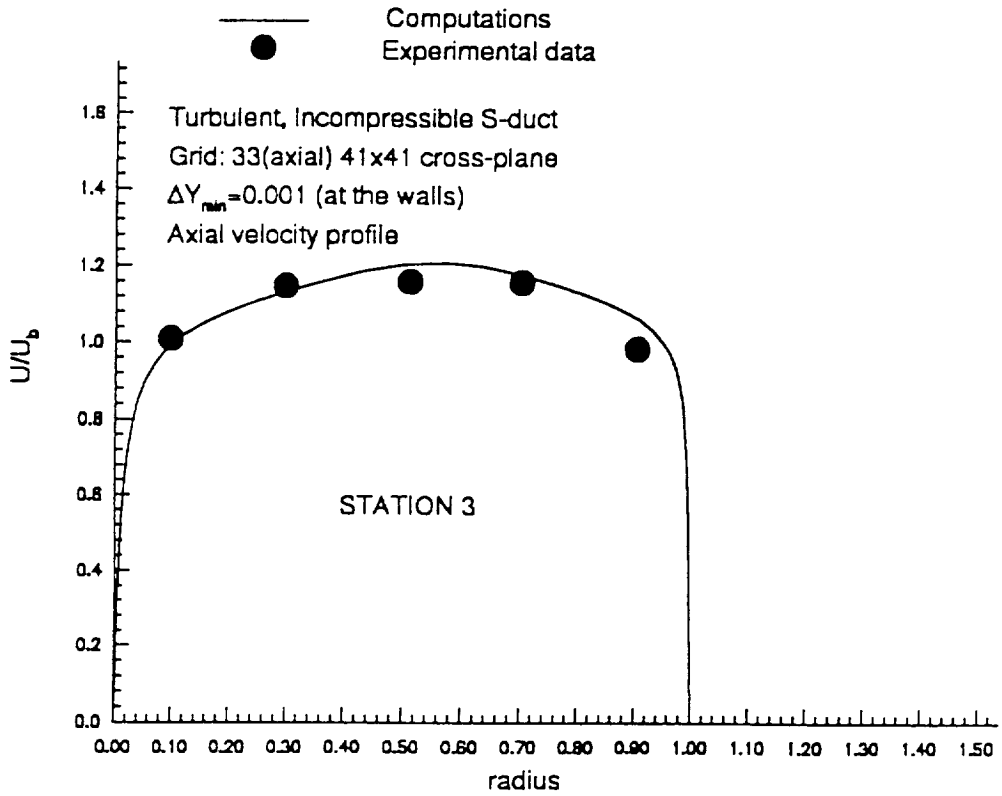
Computations
Experimental data
Turbulent, Incompressible S-duct
Grid: 33(axial) 41x41 cross-plane
ΔY_min=0.001 (at the walls)
Axial velocity profile
STATION 3
U/U_b
radius
0.0
0.2
0.4
0.6
0.8
1.0
1.2
1.4
1.6
0.00 0.10 0.20 0.30 0.40 0.50 0.60 0.70 0.80 0.90 1.00 1.10 1.20 1.30 1.40 1.50

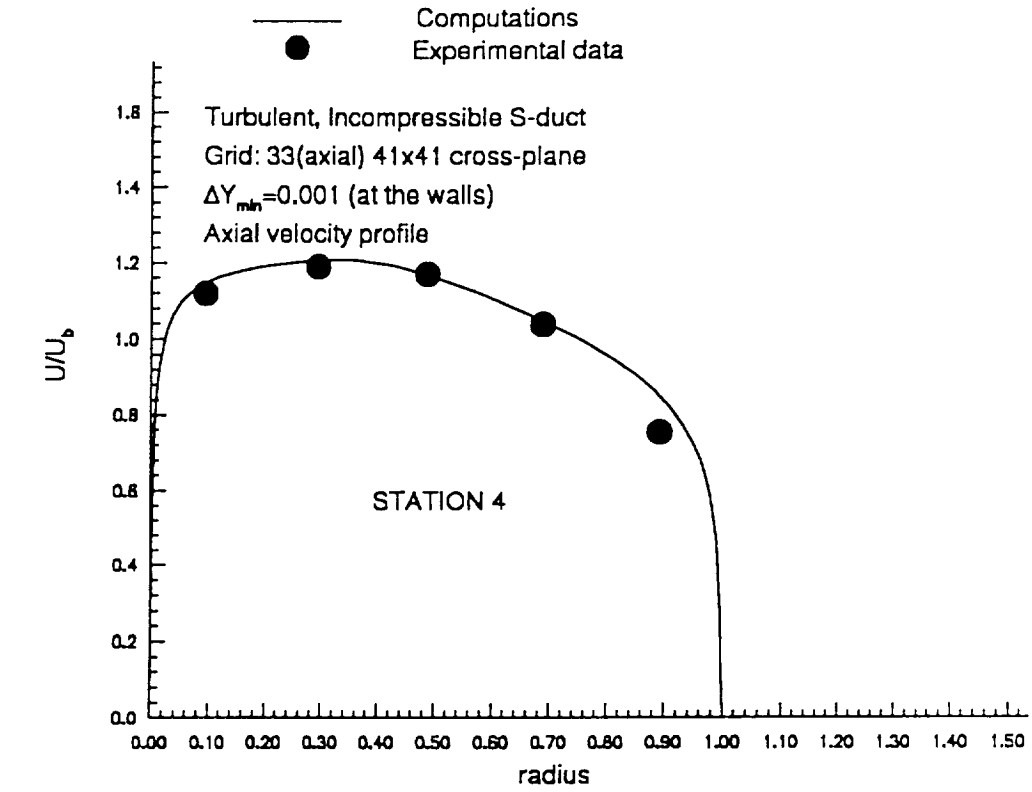

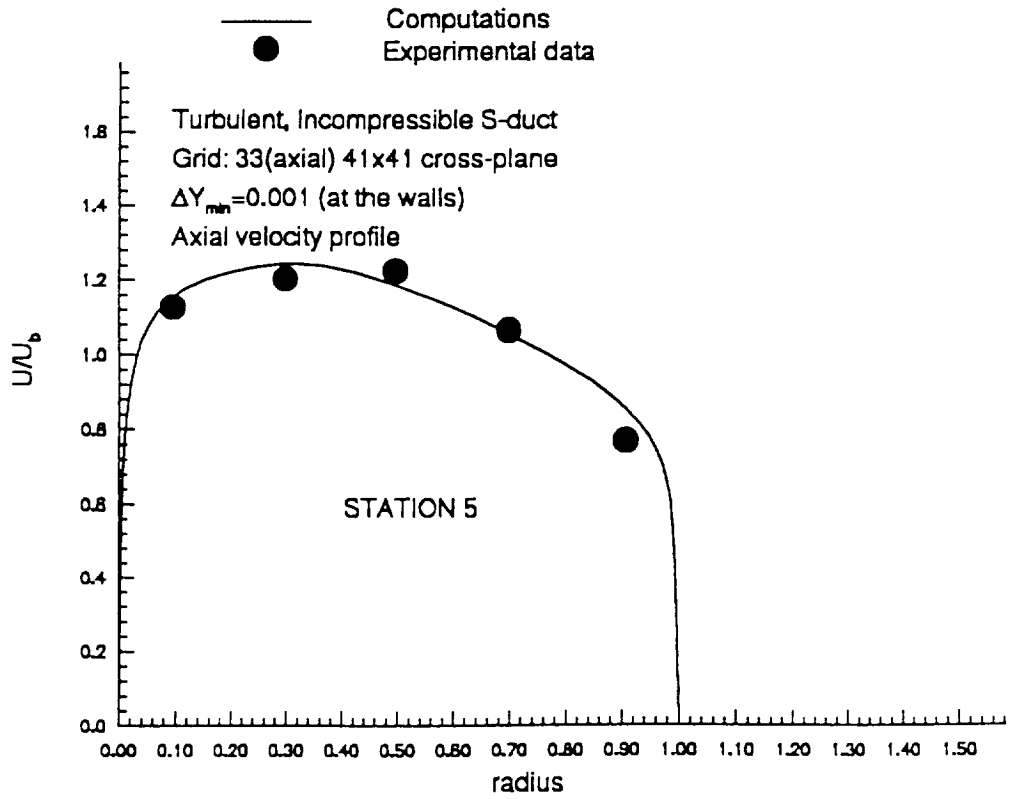

Figures 6(a-e). Comparison of the computed and measured turbulent axial velocity profiles

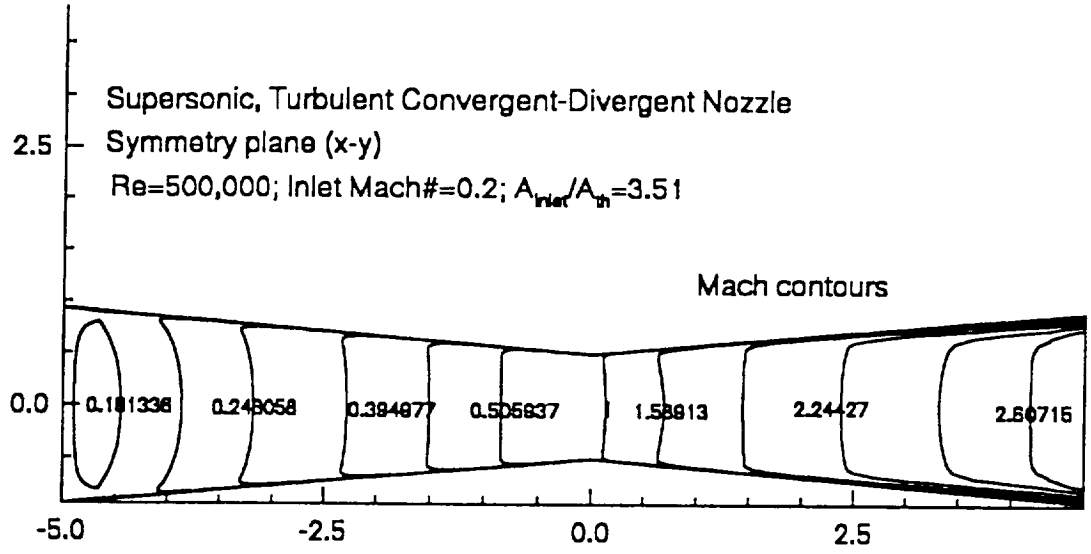

Figure 7. Mach number contours on a symmetry plane

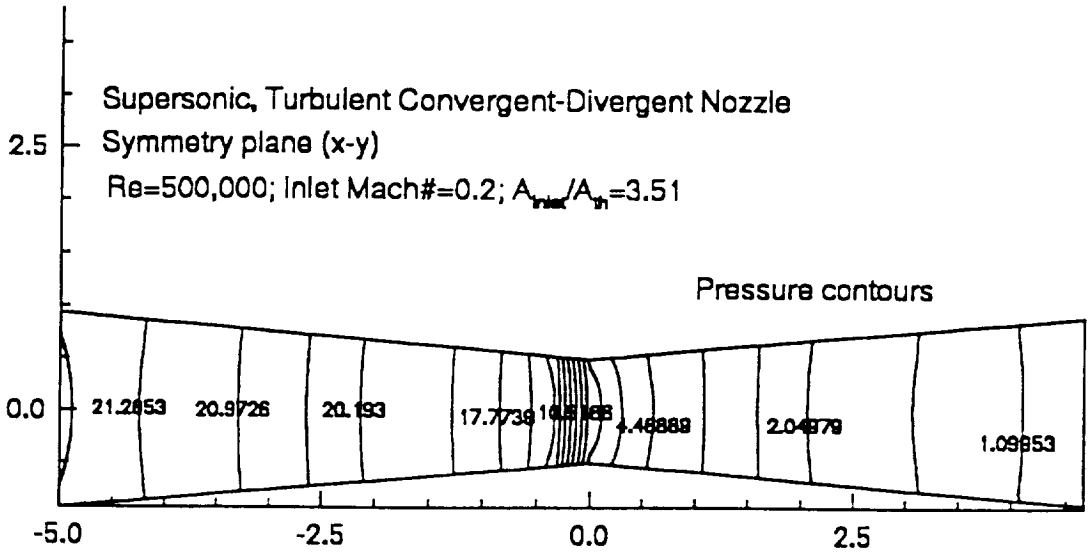

Figure 8. Non-dimensional pressure contours on a symmetry plane

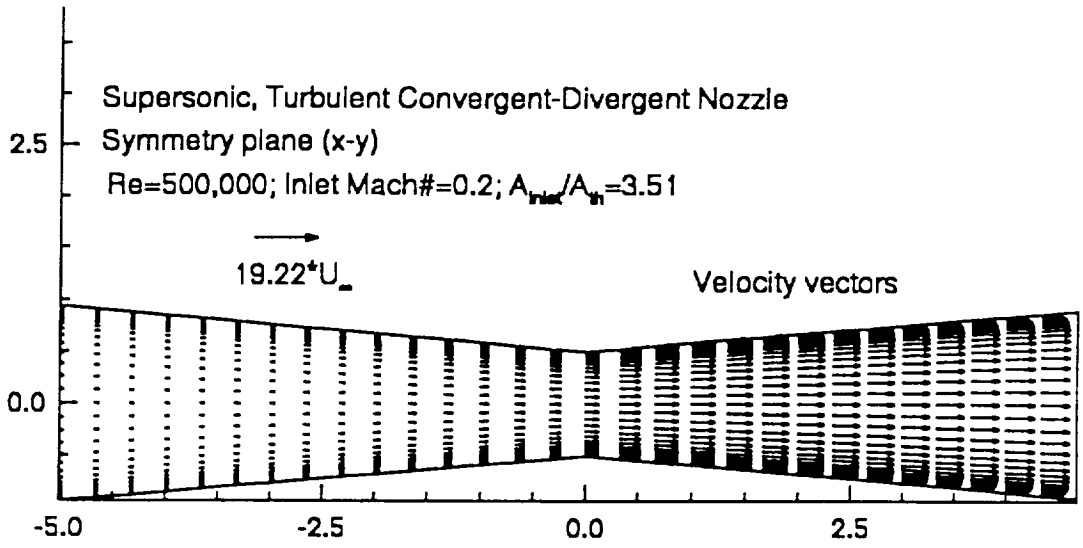

Figure 9. Velocity vectors on a symmetry plane

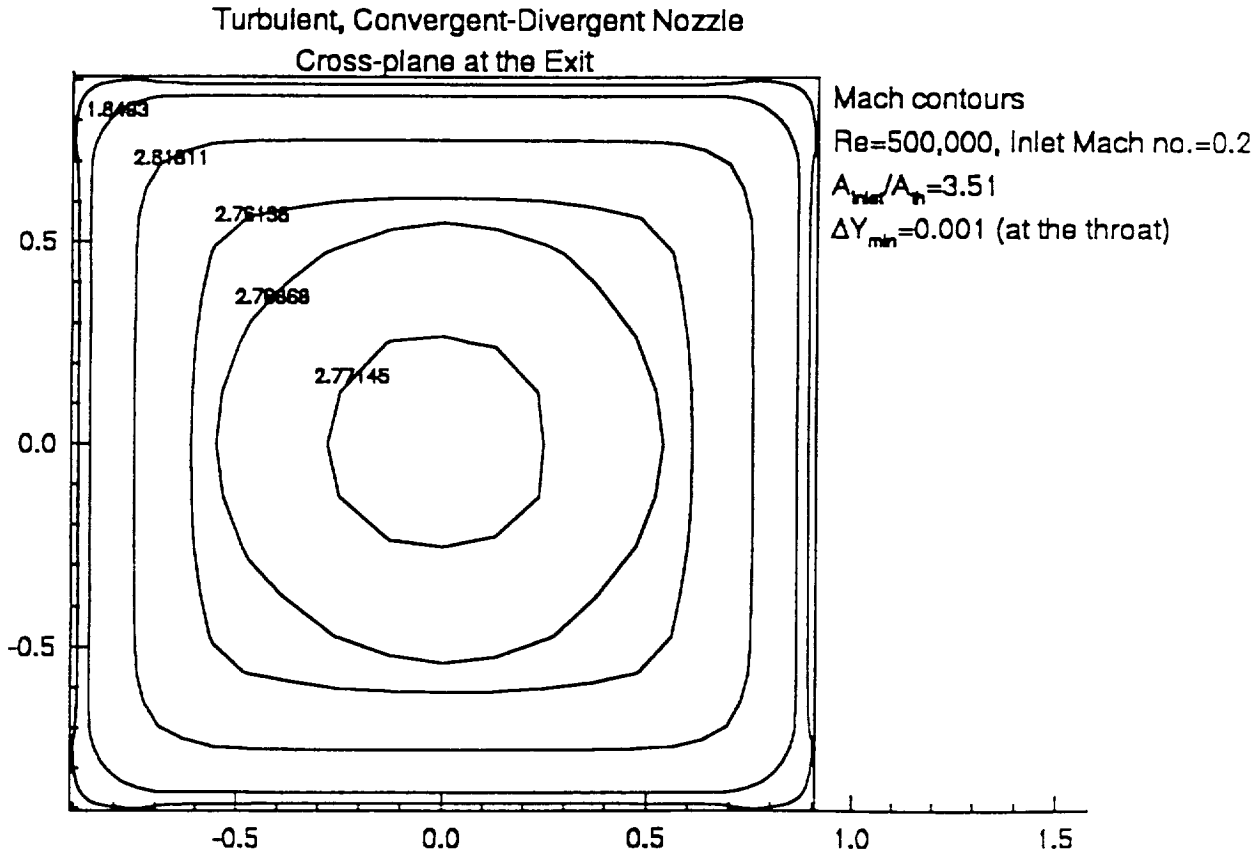

Figure 10(a). Mach number at the exit cross-plane.

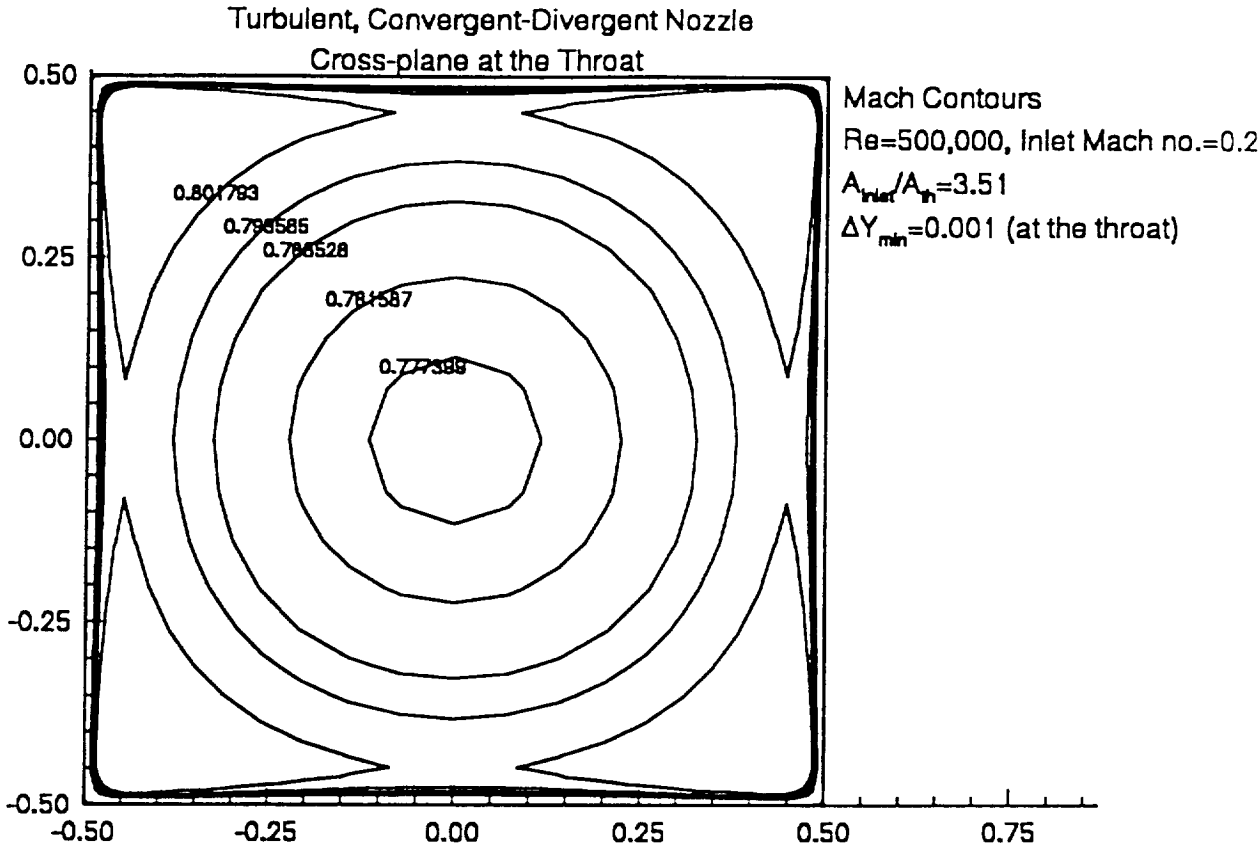

Figure 10(b). Mach number at the throat cross-plane.

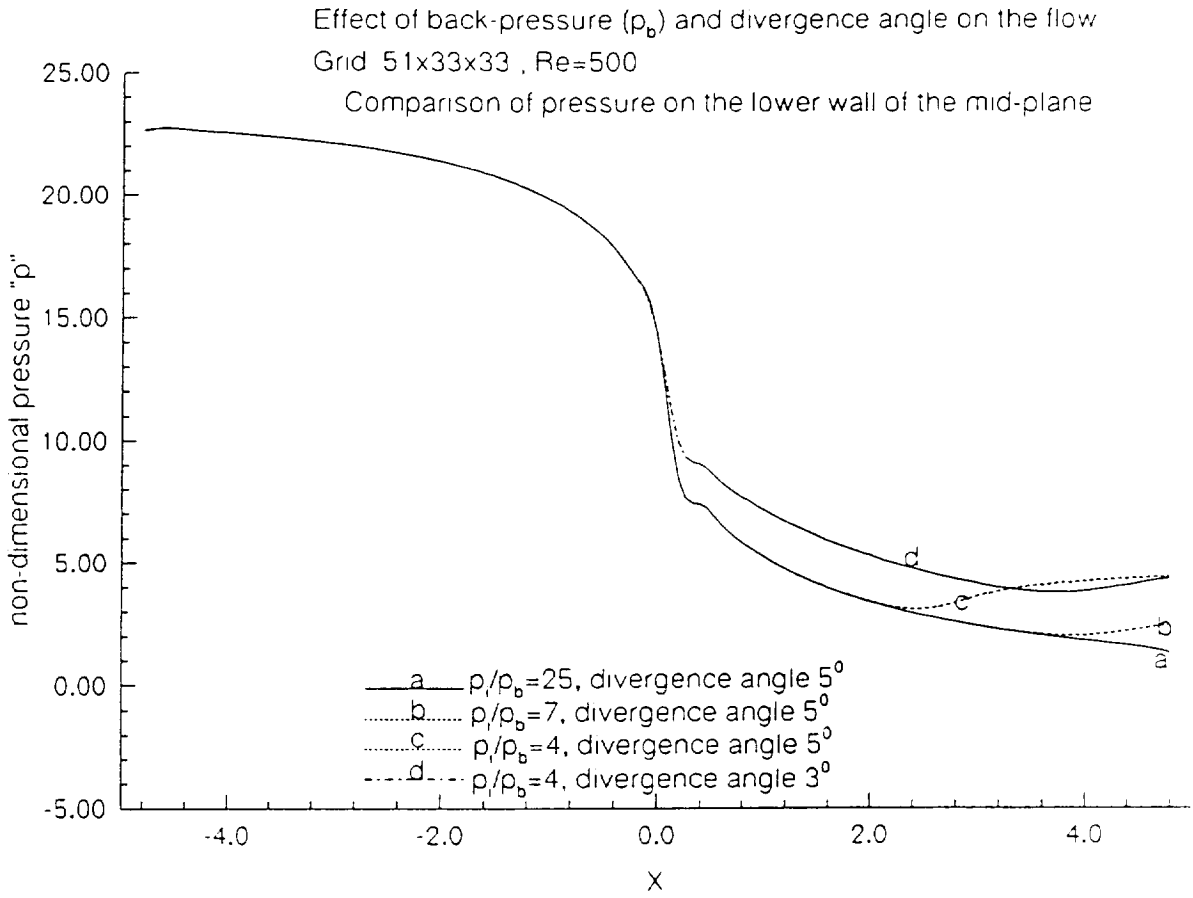

Figure 11 Comparison of pressure on the lower wall of the symmetry plane for various imposed back-pressures

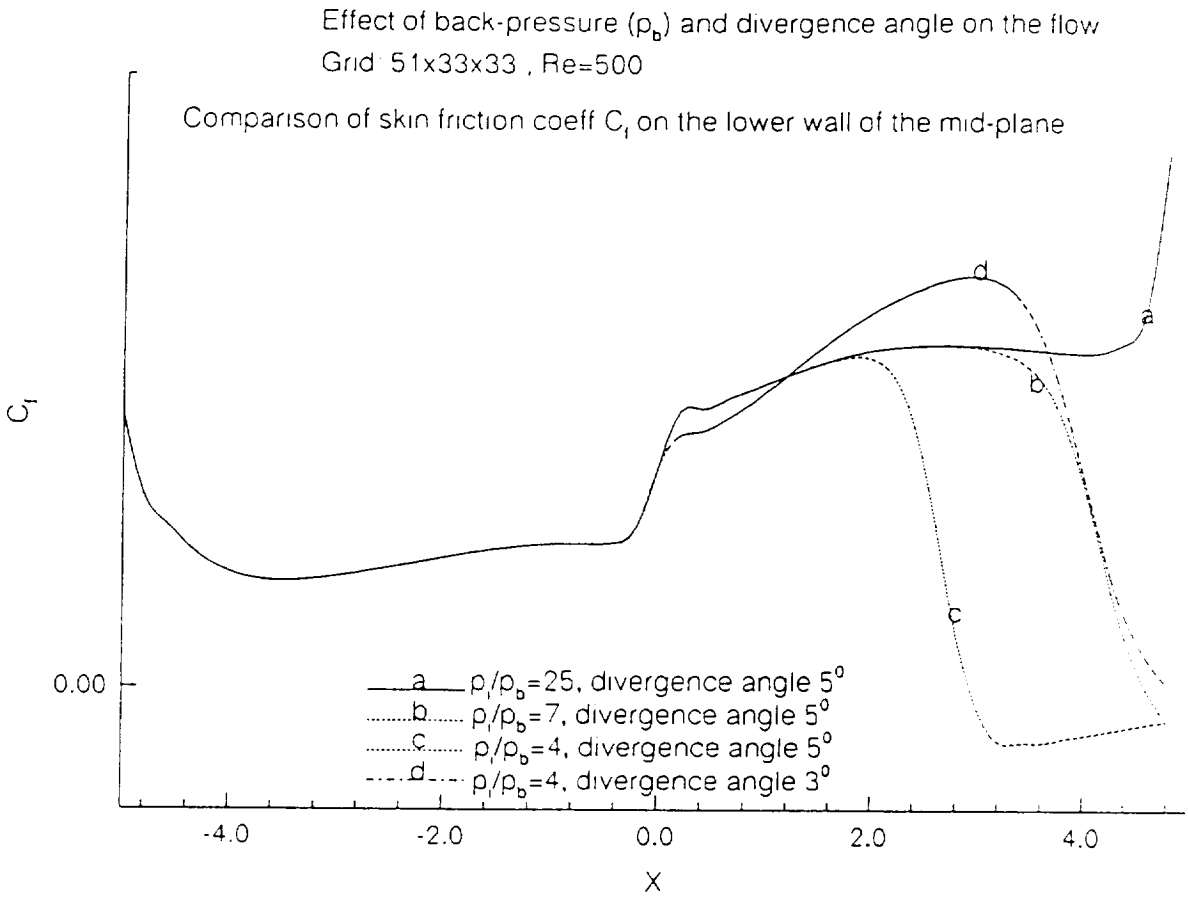

Figure 12 Comparison of skin friction coefficient C_f on the lower wall of the symmetry plane for various imposed back-pressures

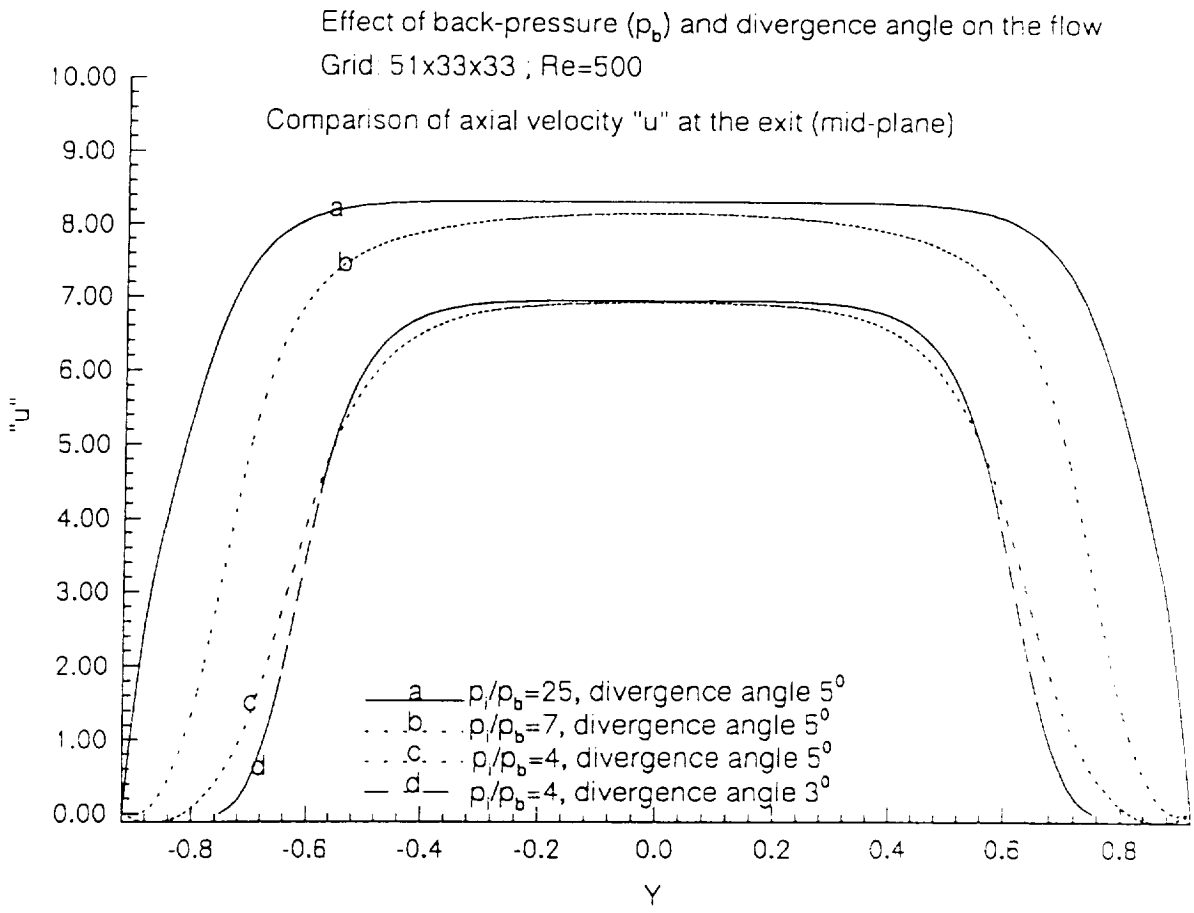

Figure 13 Comparison of axial velocity "u" at the exit cross-plane for various imposed back-pressures

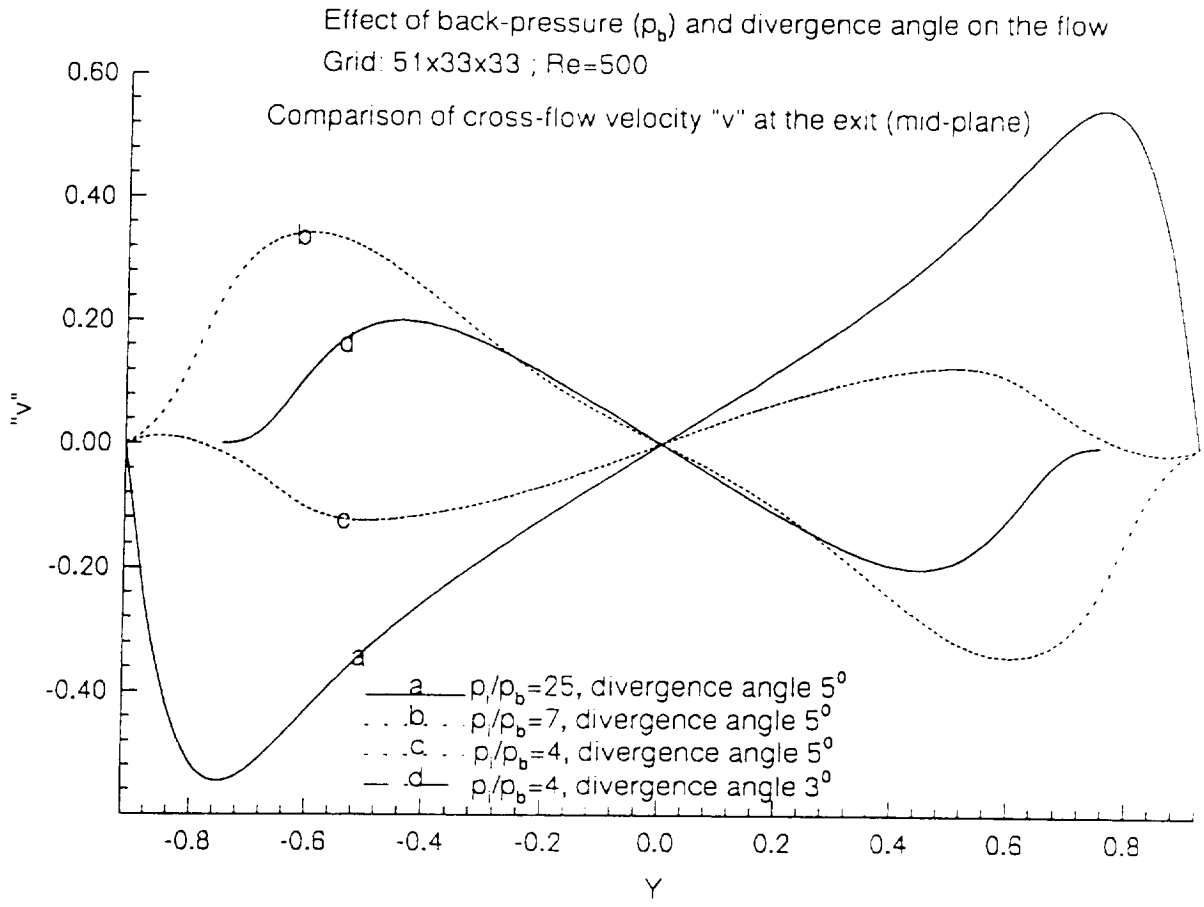

Figure 14 Comparison of cross-flow velocity "v" at the exit cross-plane for various imposed back-pressures

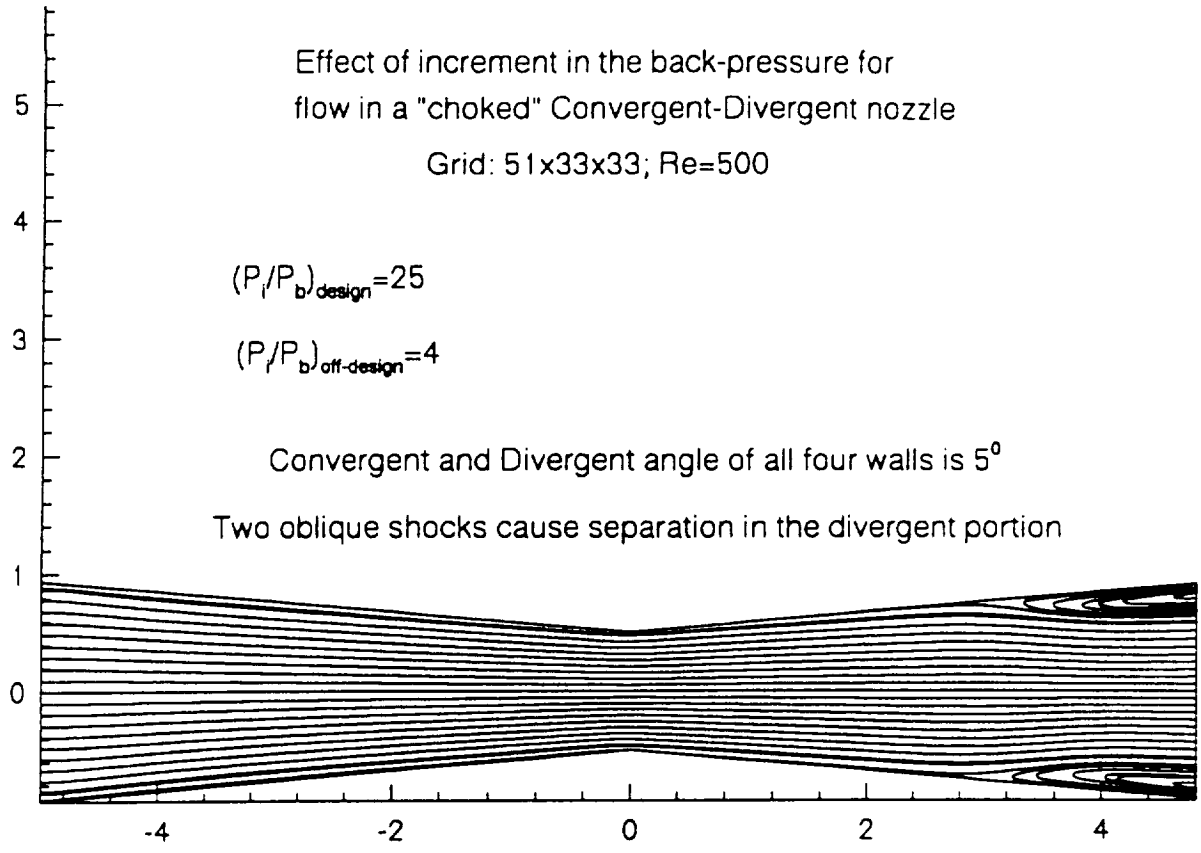

Figure 15 Streamlines on the (x-y) symmetry plane for the imposed back-pressure of p_b=6.25p_e & A_e/A_{throat} of 3.51

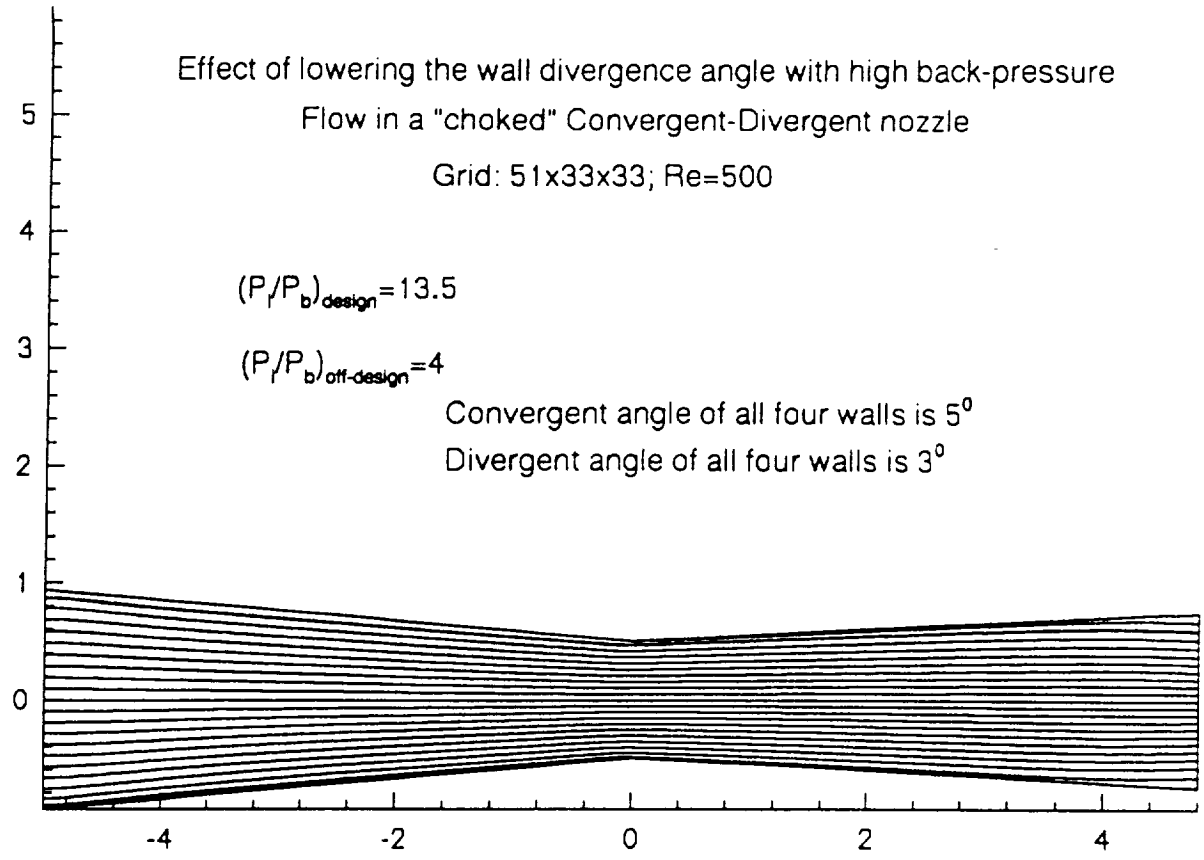

Figure 16 Streamlines on the (x-y) symmetry plane for the imposed back-pressure of $p_b=3.37p_e$ & A_e/A_{throat} of 2.3

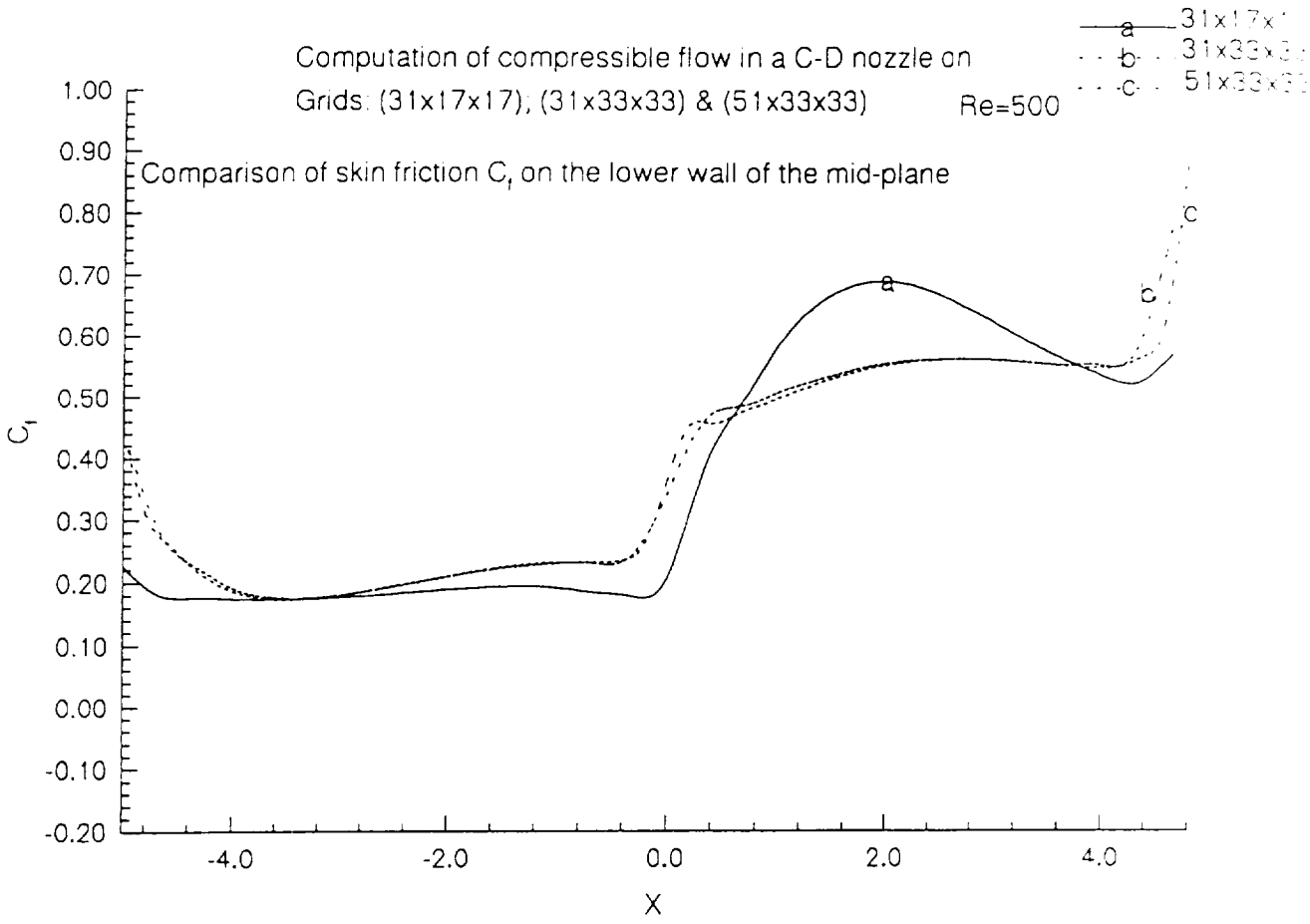

Figure 17 Skin friction coefficient C_f on the lower wall of the (x-y) symmetry plane for 31x17x17, 31x33x33 and 51x33x33 grids

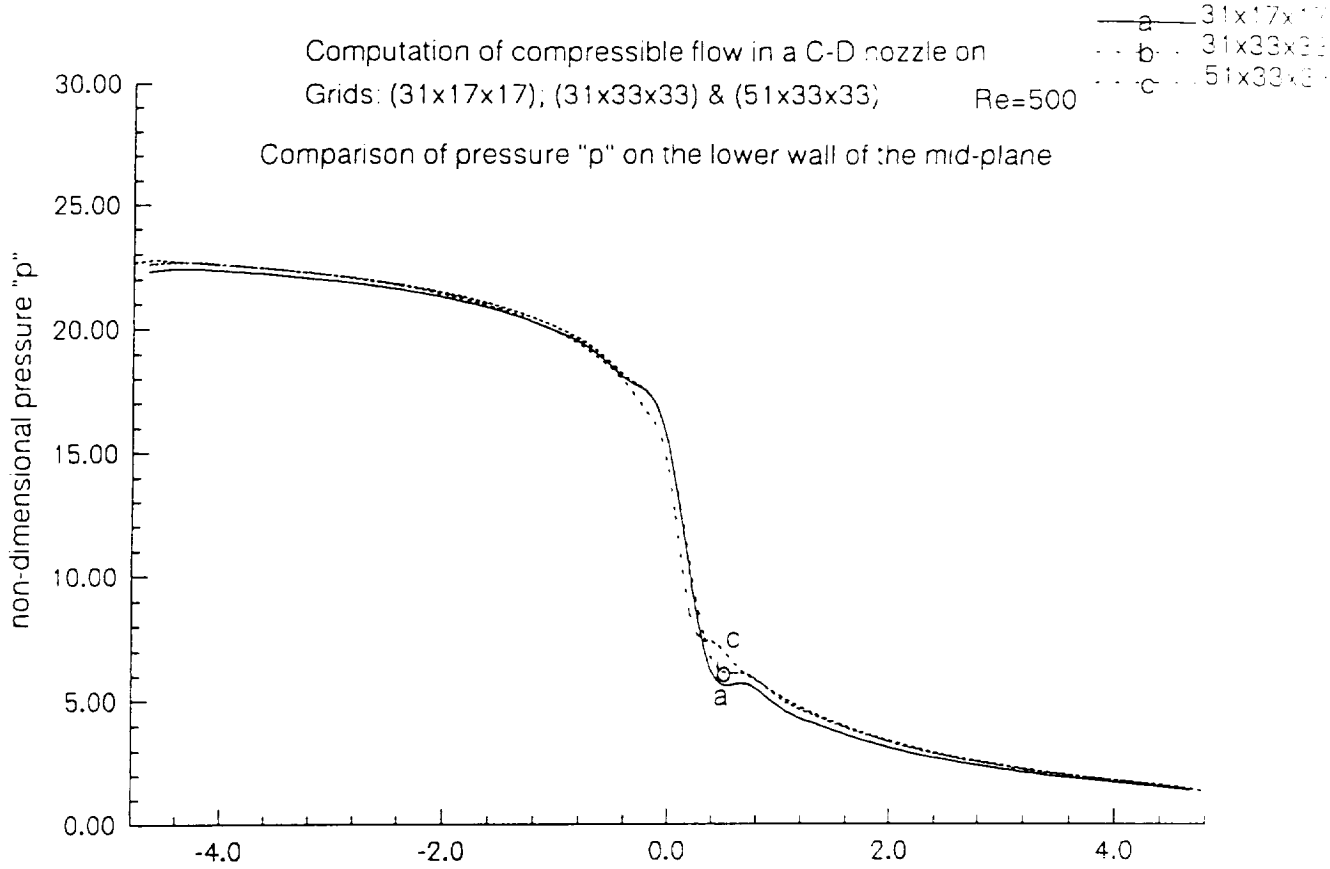

Figure 18 Non-dimensional pressure on the lower wall of the (x-y) symmetry plane for 31x17x17, 31x33x33 and 51x33x33 grids

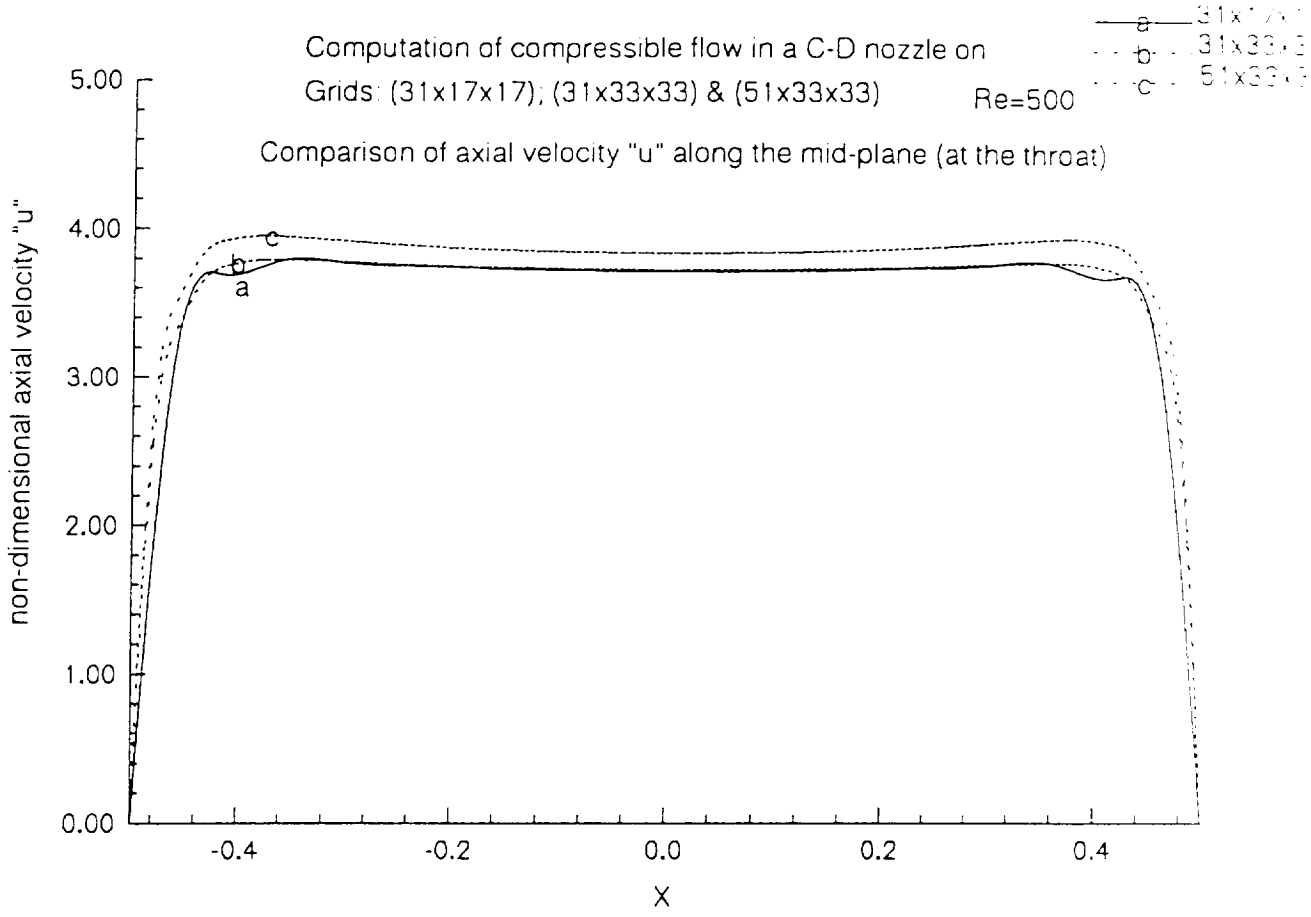

Figure 19 Axial velocity "u" at the throat for 31x17x17, 31x33x33 and 51x33x33 grids

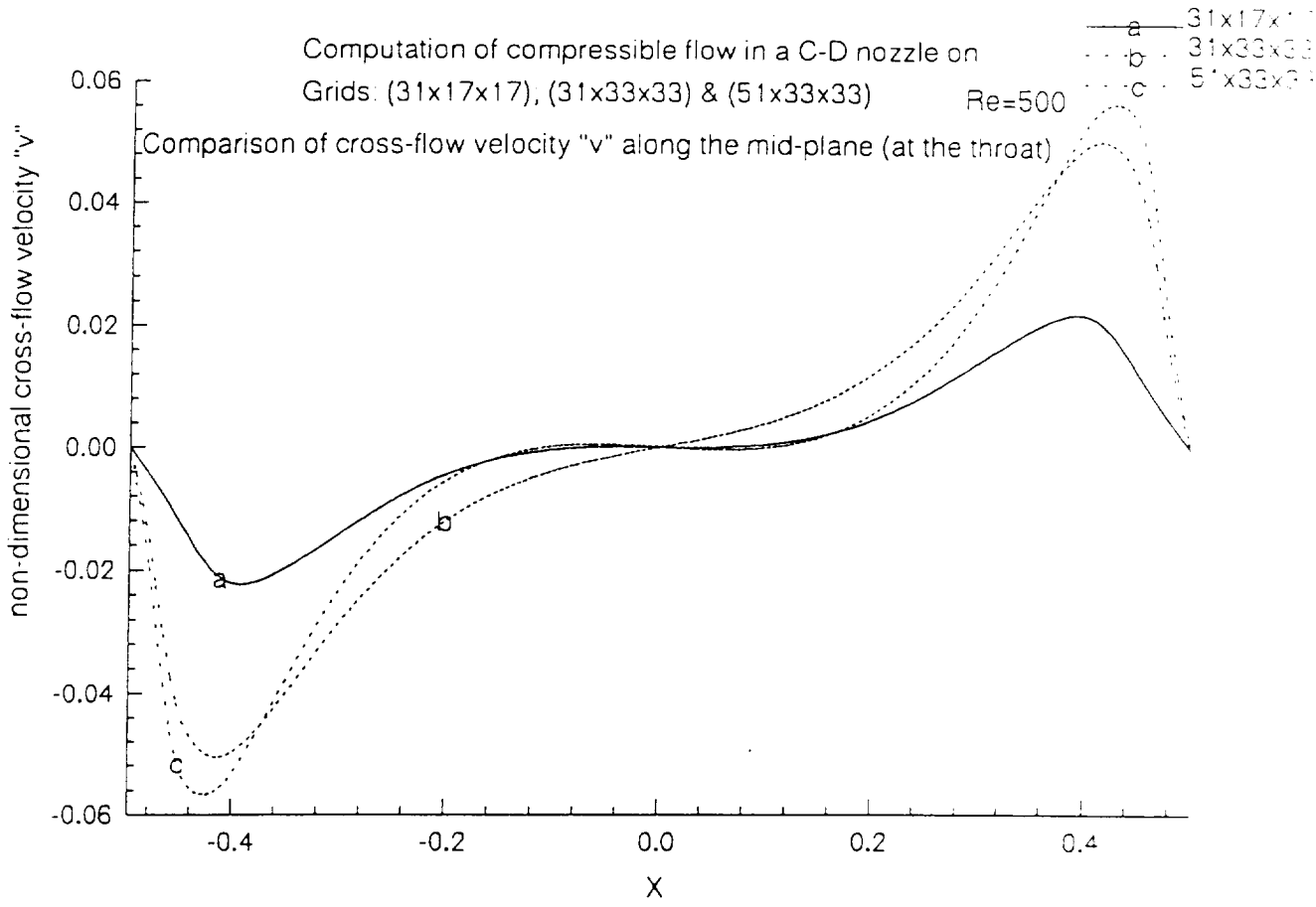

Figure 20 Cross-flow velocity "v" at the throat for 31x17x17, 31x33x33 and 51x33x33 grids

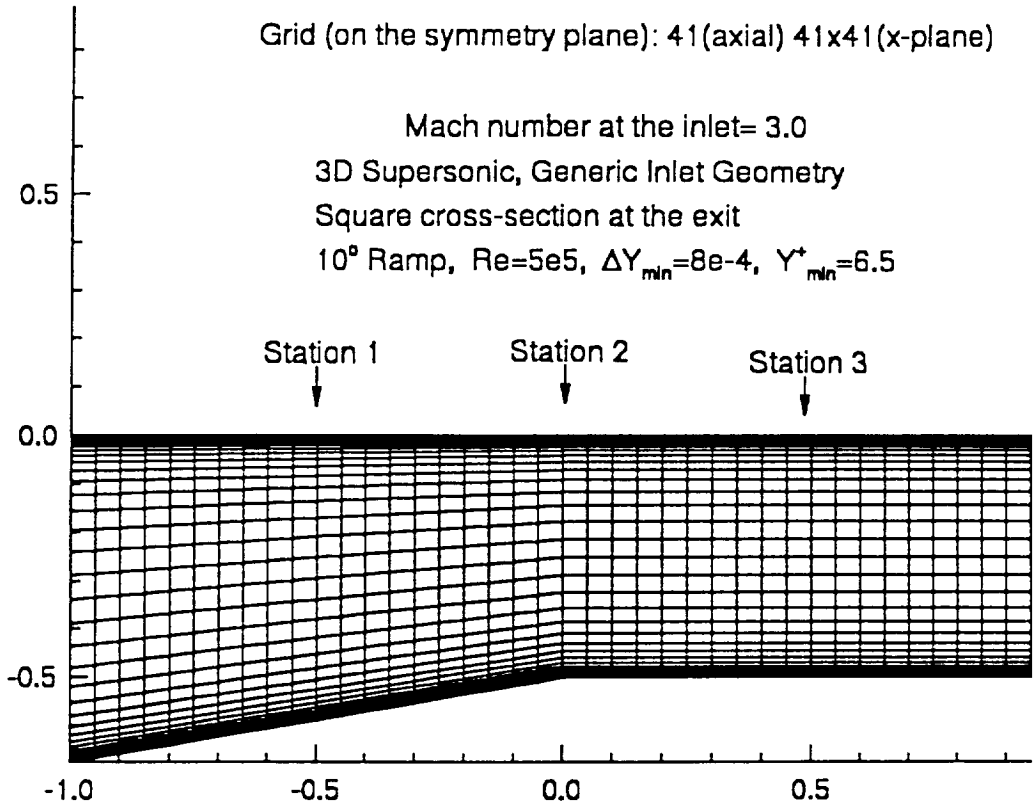

Figure 21. Typical view of the grid in the symmetry plane

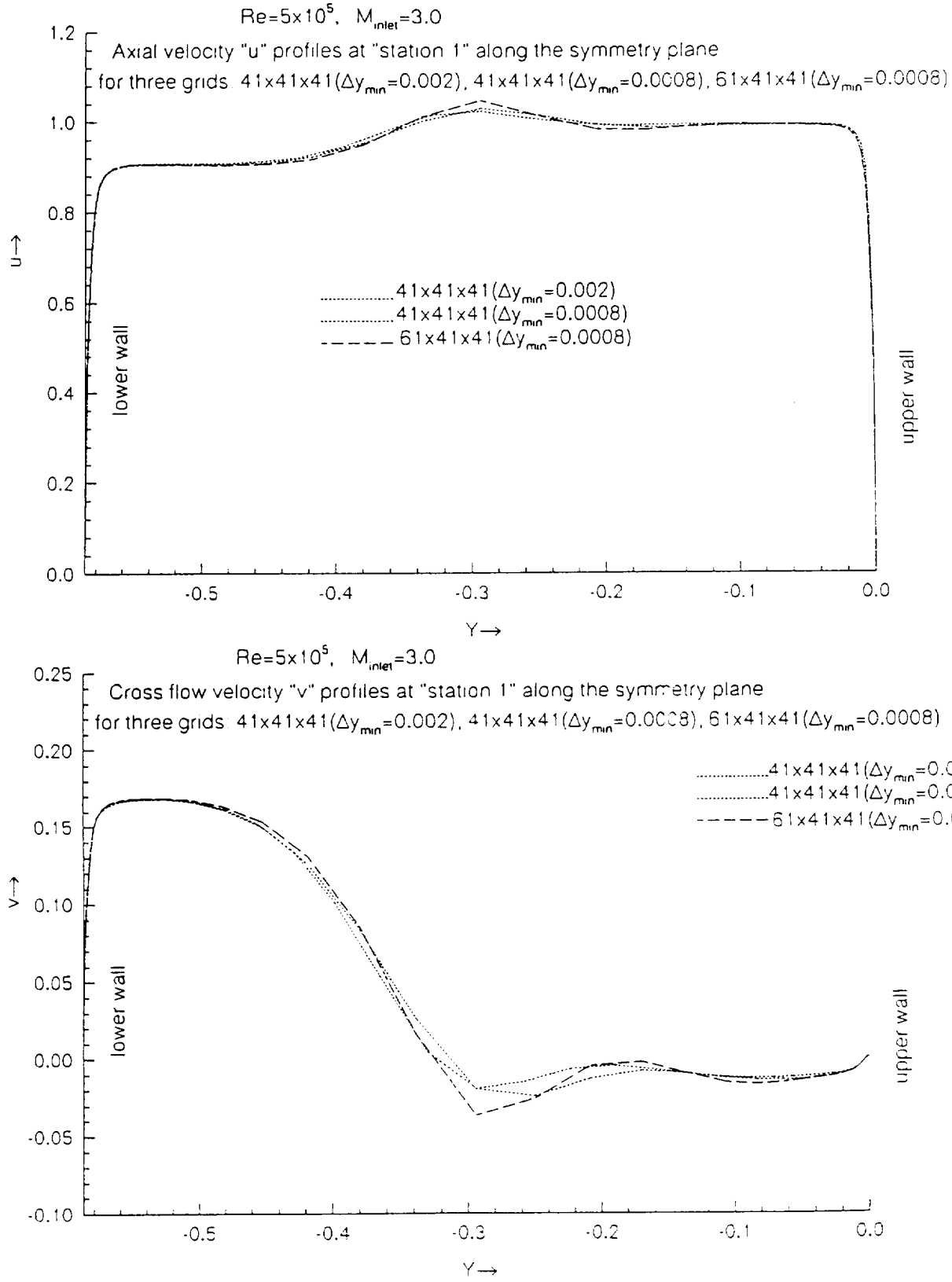

Figure 22(a-b). "u" and "v" velocity profiles at "station 1" along the mid-plane

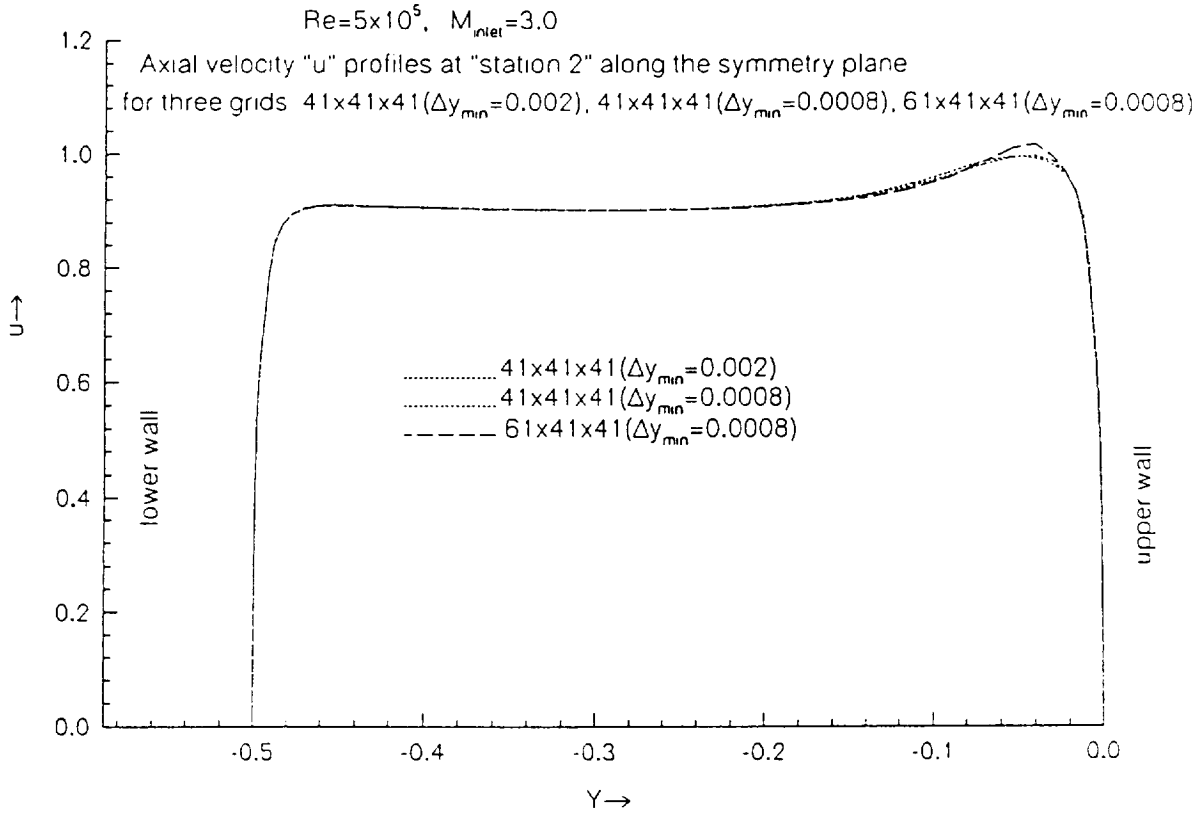
Re=5x10^5, M_inlet=3.0
Axial velocity "u" profiles at "station 2" along the symmetry plane
for three grids 41x41x41(Δy_min=0.002), 41x41x41(Δy_min=0.0008), 61x41x41(Δy_min=0.0008)
41x41x41(Δy_min=0.002)
41x41x41(Δy_min=0.0008)
61x41x41(Δy_min=0.0008)
lower wall
upper wall
u→
Y→
1.2
1.0
0.8
0.6
0.4
0.2
0.0
-0.5
-0.4
-0.3
-0.2
-0.1
0.0

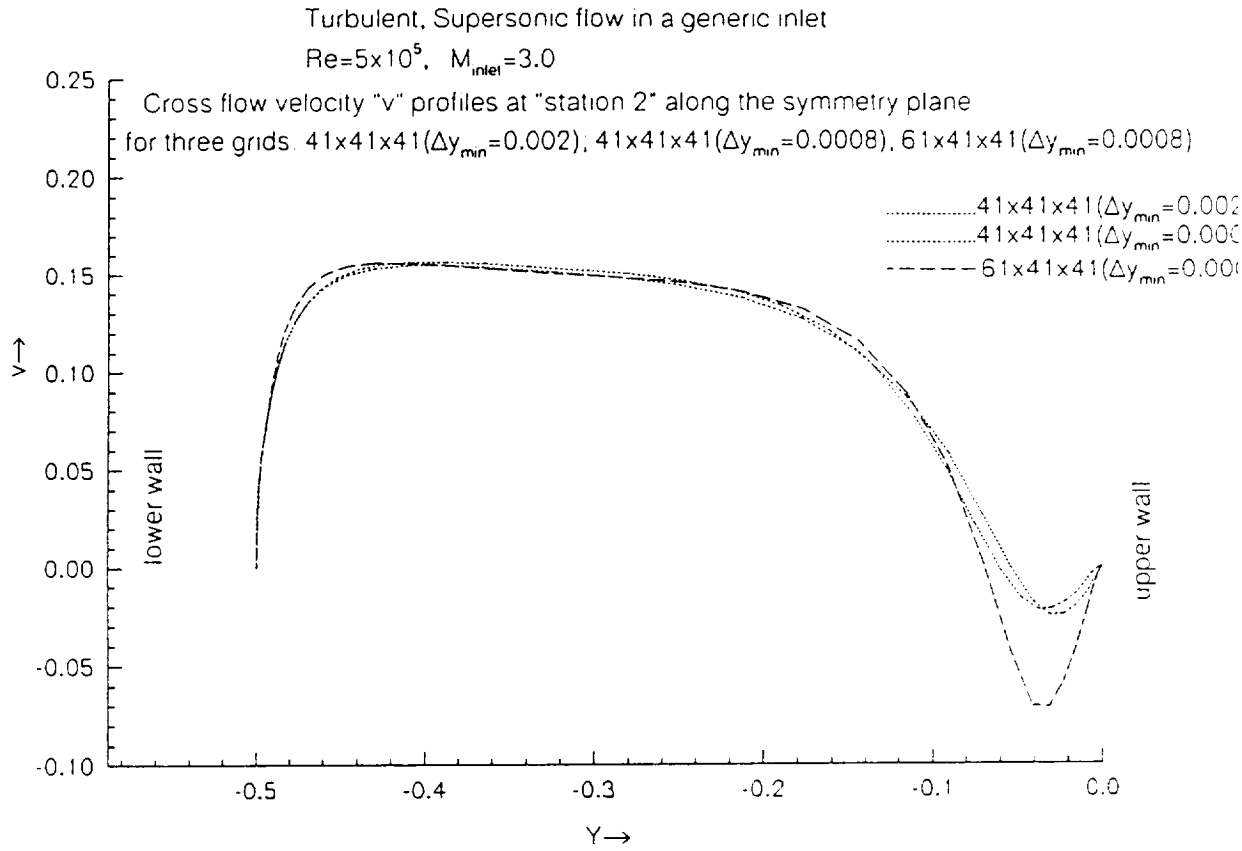

Figure 22(c-d). "u" and "v" velocity profiles at "station 2" along the mid-plane

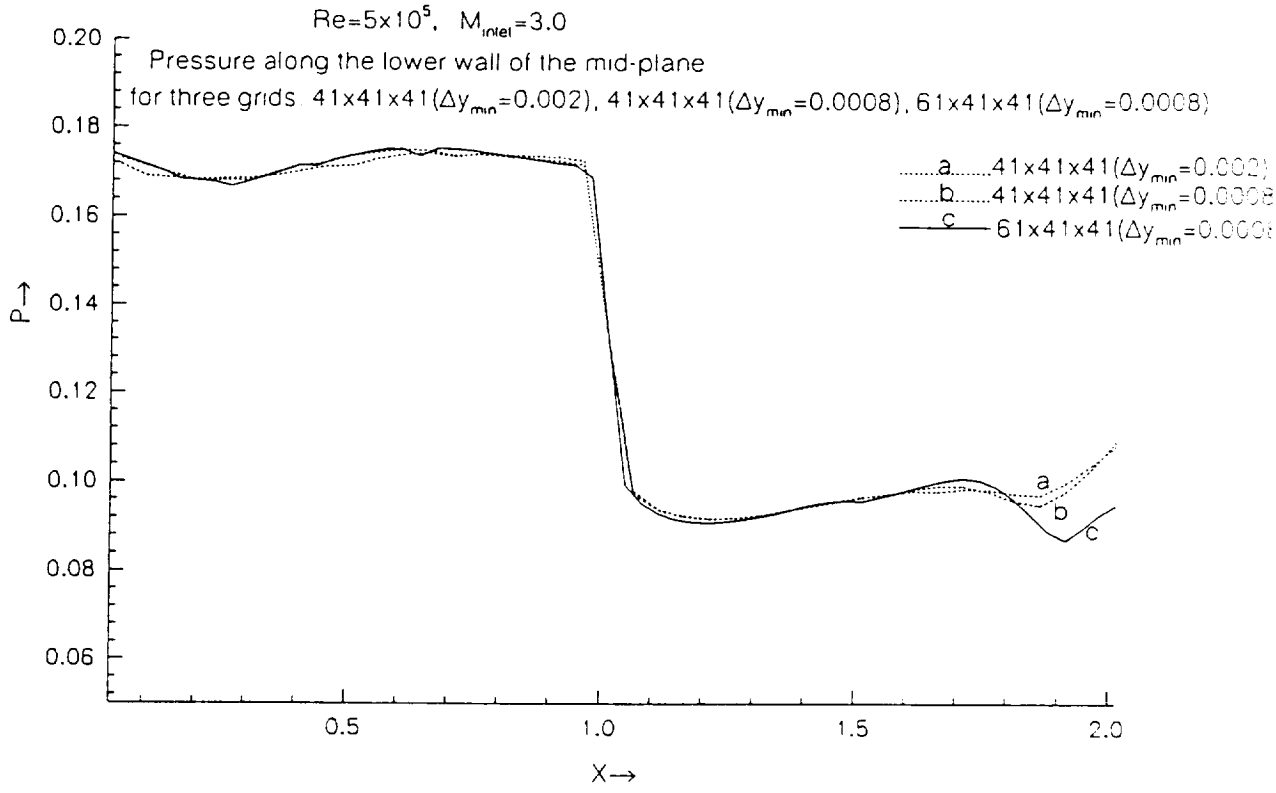
Re=5x10^5, M_inlet=3.0
Pressure along the lower wall of the mid-plane
for three grids 41x41x41(Δy_min=0.002), 41x41x41(Δy_min=0.0008), 61x41x41(Δy_min=0.0008)
a 41x41x41(Δy_min=0.002)
b 41x41x41(Δy_min=0.0008)
c 61x41x41(Δy_min=0.0008)
P→
X→
0.20
0.18
0.16
0.14
0.12
0.10
0.08
0.06
0.5
1.0
1.5
2.0
a
b
c

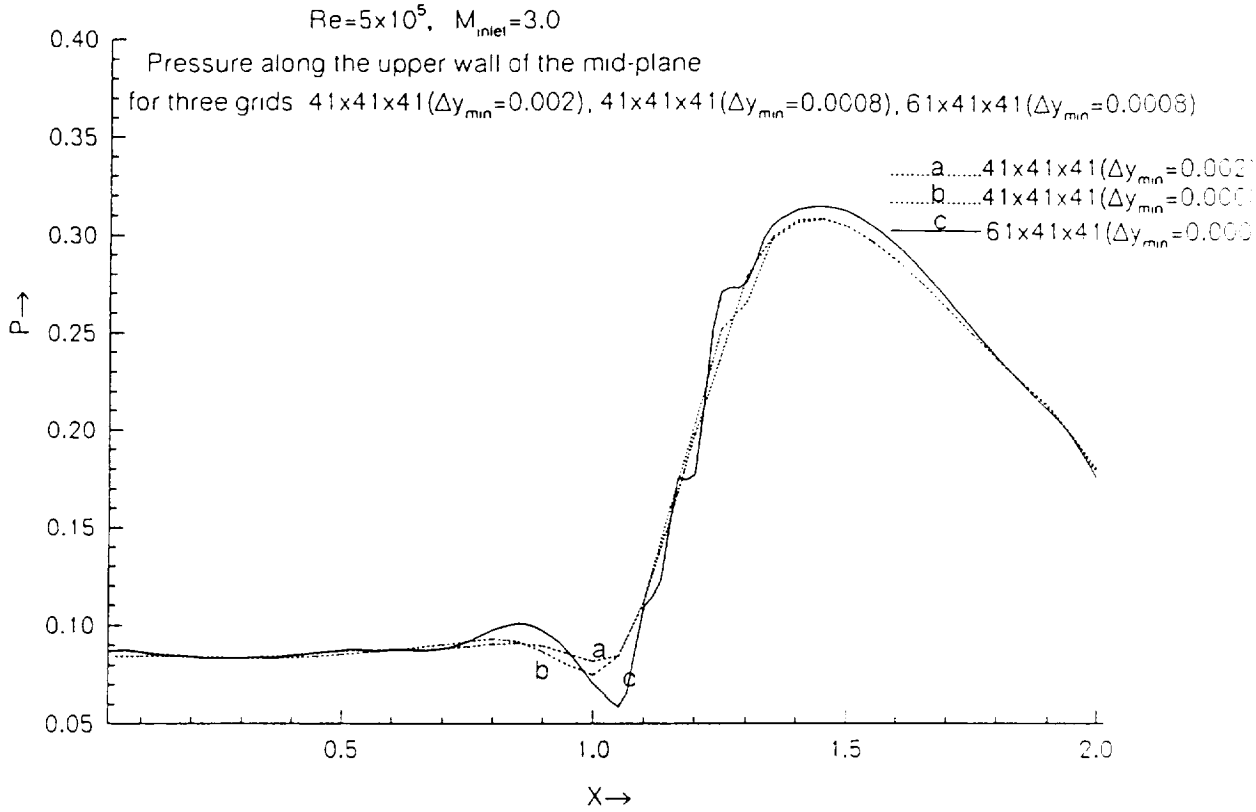

Figure 23(a-b). Non-dimensional pressure on the lower and upper walls, respectively, along the symmetry plane

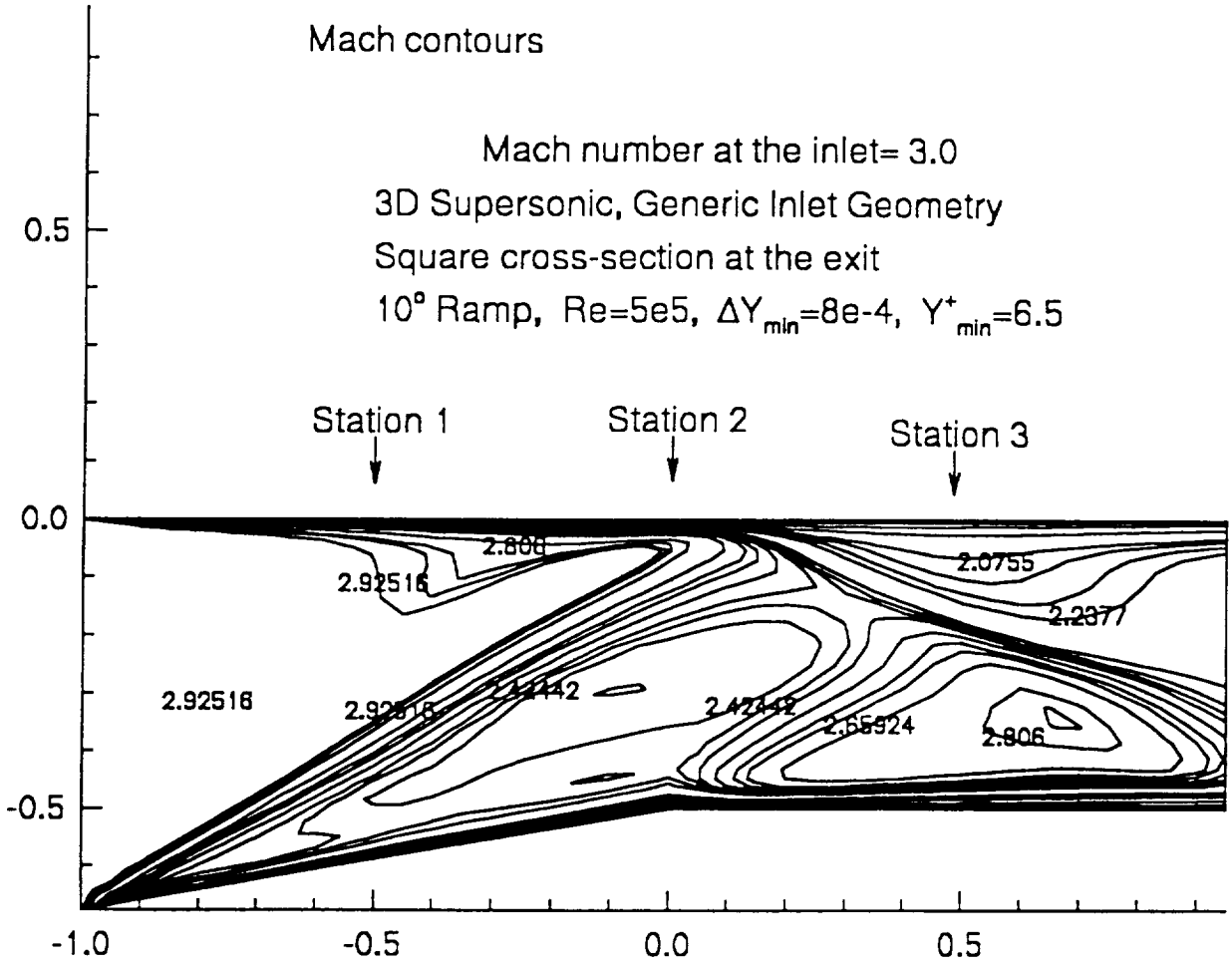
Mach contours
Mach number at the inlet= 3.0
3D Supersonic, Generic Inlet Geometry
Square cross-section at the exit
10° Ramp, Re=5e5, ΔY_min=8e-4, Y+_min=6.5
Station 1
Station 2
Station 3
0.5
0.0
-0.5
-1.0
-0.5
0.0
0.5
2.806
2.92516
2.0755
2.2377
2.92516
2.92516
2.55924
2.806